



# GNBC-based front-tracking method for the three-dimensional simulation of droplet motion on a solid surface

Xinglong Shang<sup>a</sup>, Zhengyuan Luo<sup>a</sup>, Elizaveta Ya. Gatapova<sup>b</sup>, Oleg A. Kabov<sup>b,c</sup>, Bofeng Bai<sup>a,\*</sup>

<sup>a</sup>State Key Laboratory of Multiphase Flow in Power Engineering, Xi'an Jiaotong University, Xi'an 710049, China

<sup>b</sup>Kutateladze Institute of Thermophysics, Russian Academy of Sciences, Novosibirsk 630090, Russia

<sup>c</sup>Institute of Power Engineering, National Tomsk Polytechnic Research University, Tomsk 634050, Russia



## ARTICLE INFO

### Article history:

Received 9 October 2017

Revised 19 June 2018

Accepted 27 June 2018

Available online 6 July 2018

### Keywords:

Moving contact line

Front-tracking method

Contact angle hysteresis

Generalized Navier boundary condition

## ABSTRACT

Previous front-tracking (FT) method-based models to simulate droplet motion on a solid surface with a moving contact line (MCL) are limited to two-dimensional models in which the Navier boundary condition (NBC) is employed for the MCL. In this paper, we develop a three-dimensional FT method that integrates the generalized Navier boundary condition (GNBC) to model the MCL. This GNBC-based FT method addresses several key issues, such as the integration of GNBC for the dynamic description of the MCL and its coupling with the surrounding flow, the accurate updating of the density and viscosity of the two-phase fluid near the contact line, and the restructuring of the Lagrangian mesh for tracking the drop surface, especially near the contact line. The stability and accuracy of the present numerical method are validated by several tests: (1) numerical performance tests, (2) simulation of the transient and steady-state shapes of droplets under flow with a fixed contact line, and (3) simulation of a droplet spreading under gravity and moving under a shear flow with MCLs. Excellent agreement is achieved between the results obtained by our model and the data obtained by other theoretical and numerical approaches.

© 2018 Elsevier Ltd. All rights reserved.

## 1. Introduction

The motion and deformation of droplets on a solid surface under flow are of fundamental interest in nature and in industrial applications [1–3], such as coating operations, enhanced oil recovery and droplet manipulation in microfluidic devices [4]. In microfluidics, droplet sliding on a solid surface is commonly used to produce monodisperse droplets as transport vehicles or chemical reaction containers. In the petroleum industry, the effectiveness of enhanced oil recovery techniques is strongly dependent on the displacement and detachment of small oil droplets attached to solid surfaces, and the interaction between crude oil and the displacing fluid is extremely complex. In addition, patterning a solid surface with elaborate wettability can allow control of or even drive droplet motion on the solid surface. Investigating droplet motion on a solid surface and the underlying mechanisms is of great importance and is motivated by the continuous development of these aforementioned applications.

The mechanical behavior of droplets on a solid surface under flow has gained extensive attention due to its significant scientific interest. The motions of droplets on solid surfaces are gov-

erned by various forces, including interfacial forces, viscous forces, gravity and inertial forces. When the surface-to-volume ratio of the droplet is large, e.g., for droplets moving in confined microchannels, the droplet motion is strongly influenced and even dominated by interfacial forces. Under these conditions, in addition to considering the surface tension of the liquid interface, the capability of describing the interaction between the droplet and the solid surface becomes imperative to the success of any attempt to model such a system. More complexities, such as contact angle hysteresis (CAH), often arise in practice due to the influence of surface roughness and heterogeneities. These complexities may cause the flow-induced motion and deformation of droplets, resulting in complex patterns, such as stick-slip motion. Although the macroscopic behavior of interfacial deformation near the contact line has been successfully observed and described in many cases in the literature [1,3], a complete mathematical representation of the motion of droplets on a solid surface remains a formidable task, especially for a three-dimensional system that accounts for the complex behavior of a moving contact line (MCL).

The presence of the MCL complicates the already challenging task of the numerical simulation; in the continuum approach that solve numerical approximations of the full Navier-Stokes equations, well-grounded physical modeling of MCLs is required. In addition to accounting for the elimination of stress singularities, an

\* Corresponding author.

E-mail address: [bfbai@mail.xjtu.edu.cn](mailto:bfbai@mail.xjtu.edu.cn) (B. Bai).

appropriate mathematical formulation that incorporates the interfacial physics effects associated with the solid surface must be enforced in those numerical simulations. Many attempts have been made to remove stress singularities: in addition to introducing the dissipation term in the governing equations, the most common approach is to replace the no-slip boundary condition by using a slip model near the contact line, such as the Navier boundary condition (NBC) [5]. However, a boundary condition for the contact angle is still necessary to close the hydrodynamic equation. In general, the NBC is generally applied either in association with a prescribed dynamic contact angle or as part of more generalized boundary conditions that introduces only an energy scale. The other mechanisms that are commonly used in combination with continuum hydrodynamics can be found in the review article of Sui et al. [2]. Other empirical MCL models in terms of the dynamic contact angle have also been proposed to describe the behavior of the contact line, such as Kistler's model [6], Jiang's model [7] and the Hoffman–Voinov–Tanner model [6]. In general, these models should be accompanied by a boundary condition for the velocity field to solve the stress singularity at the contact line, as described above. Most of the models are only reasonable for specific systems (e.g., gas–fluid–solid system) and cannot be directly extended to cases that consider the complex liquid–liquid interfacial properties, including viscoelasticity and other adhesion forces. Recently, Qian et al. [8] determined that the relative slippage between the fluids and the solid surface everywhere follows the generalized Navier boundary condition (GNBC), in which the amount of slippage is proportional to the sum of the tangential viscous stress and the unbalanced Young's stress induced from the deviation of the fluid–fluid interface from its equilibrium configuration. The complex interfacial physics can be directly considered by modifying the interfacial source term in the GNBC. Other elaborate MCL models have also been developed to consider the effects of surfactants [9] and heterogeneous [10,11] and structured [12–14] solid surfaces. Most MCL models can be applied or adapted in simulations using a coefficient extracted from experimental data to prescribe the contact angle or contact line speed. The main limitation of these models is that they do not consider the characteristics of the solid surface [15]. Despite the respective advantages of different two-phase flow methods and the crucial issues solved by the introduction of MCL models, implementing these models in a stable and precise manner remains a challenge, especially in three-dimensional simulations.

In addition to describing contact line movement, numerical methods should also consider the deformation of interface from the surrounding fluid. Most of the numerical methods that are widely used for capturing/tracking deformable interfaces already consider the MCL, such as the VOF [16,17] and level-set [18,19] methods. Although the MCL models used in these methods differ, a slip model (e.g., NBC) in conjunction with a relation related to the contact angle is generally imposed on the contact line. The contact line is directly advected either by imposing a prescribed dynamic contact angle or by identifying the contact line speed. Ding et al. [20], Ding and Spelt [21] used a diffuse-interface method to modeling the MCL. A diffuse interface is considered near the contact line, which also results effectively in slip through the diffusive fluxes between the two fluids. This method can remove the stress singularity at the contact line even when a no-slip velocity boundary condition is imposed. However, the sharp interface limit remains the subject of active debate [22].

Recently, the front-tracking (FT) method has also been extended to simulating flow problems involving the MCL. This method distinguishes itself by tracking the deformed interface and thus can achieve, in general, an accurate representation of geometric interfacial quantities (i.e., interfacial force and contact angle). Therefore, it is convenient to implement MCL models to account for

the complex interfacial physics associated with the contact line. Li et al. [23] introduced an augmented variable along the solid surface in the immersed boundary method to satisfy the stress balancing boundary condition. Zhang et al. [24] used a slip boundary to model the motion of the contact line in the FT method, but a constant contact angle was applied. Manservisi and Scardovelli [25] and Muradoglu and Tasoglu [26] used the interpolated contact angle determined by the MCL model to update the contact line shape in the FT method, in which precise implementations of the surface tension and local mass conservation were adopted. Huang et al. [27] introduced local forces on the contact line in the governing equations based on a linear relation. Yamamoto et al. [28] proposed an FT method using the stress-based GNBC to determine the contact line speed, and the calculation resulted in a very stable and reasonable flow field near the contact line in a capillary tube.

Available FT methods for simulating the MCL problem are two-dimensional, and three-phase approaches with NBC rarely achieve the generality and flexibility necessary for computational formulations to describe the complex motion of the contact line. Although previous studies have claimed that the extension of two-dimensional FT methods to three dimensions is straightforward, restructuring the deformed interface for three-dimensional flows remains a challenge, especially for cases that must account for topology changes of the fluid interfaces. In the three-dimensional case of an interface touching a solid surface, in addition to numerical challenges in integrating the accurate modeling of contact line dynamics for three-dimensional interface simulations, it is also necessary to ensure the precise tracking of the contact line evolution on the solid surface. First, the correct transition of the material field is needed to obtain a reasonable flow field where the interface crosses the solid surface. Furthermore, a high-quality Lagrangian mesh is also indispensable, especially in the calculations of forces and the contact angle at the contact line for three-dimensional simulations. The poor-quality triangular mesh that appears at the local interface, especially for the region close to the contact line, should be alleviated via surface mesh optimization algorithms. Furthermore, it is relatively straightforward to implement MCL models and automatically track the contact line explicitly along the dynamic contact angle. Therefore, there is an unmet need to develop an elaborate three-dimensional FT method that accounts for the complex interfacial physics involving the MCL.

In this paper, we propose a full three-dimensional model for the simulation of droplet motion on a solid surface in which the FT method combined with GNBC is used to track the deformed droplet interface and the movement of the contact line. Several key issues in integrating the GNBC with the FT method are solved. A boundary condition for velocity on the solid surface, considering the effects of wettability, is constructed based on the GNBC, in which the tangential friction in the contact line region is converted to a slip velocity as a boundary condition to solve the momentum equation. More importantly, as the indispensable premise for precisely tracking the contact line evolution for three-dimensional simulation, the unbalanced Young's stress is accurately represented using the explicit Lagrangian mesh with high quality, as guaranteed by implementing interface restructuring and feature-preserving optimization algorithms. Then, to obtain the accurate slip velocity on the solid surface near the contact line, the indicator function is modified using a vector function related to the dynamic contact angle. A variety of numerical tests were performed to examine the numerical performance and accuracy of our method.

## 2. Formulation

We previously developed a three-dimensional FT/finite-difference method to study the deformation and motion of

elastic capsules freely suspended in shear flows [29–31]. In this paper, we further integrate the GNBC [8,32] into the FT method to model the motion of droplets on solid surfaces with a MCL. The mathematical formulation is briefly described in this section. A single set of Navier–Stokes equations is employed to govern the incompressible two-phase flow over the entire computational domain as follows:

$$\nabla \cdot \mathbf{u} = 0, \quad (1)$$

$$\frac{\partial(\rho\mathbf{u})}{\partial t} + \nabla \cdot (\rho\mathbf{u}\mathbf{u}) = -\nabla p + \nabla \cdot \mu(\nabla\mathbf{u} + \nabla\mathbf{u}^T) + \int_A \sigma\kappa\mathbf{n}_f\delta(\mathbf{x} - \mathbf{x}_f)dA, \quad (2)$$

where  $\mathbf{u} = (u, v, w)^T$  is the velocity vector,  $t$  is the time,  $p$  is the pressure, and  $\mu$  and  $\rho$  are the discontinuous viscosity and density field of the two-phase fluids, respectively. The last term in Eq. (2) represents the interface force due to surface tension at the interface  $A$ , where  $\sigma$  is the surface tension coefficient,  $\kappa$  and  $\mathbf{n}_f$  are the curvature and the outer unit vector normal to the interface segment with area  $dA$ . The surface tension term in the right hand of Eq. (2) is obtained from the Lagrangian grid points and is distributed to the surrounding Eulerian grid points using a smoothed approximation of the Dirac Delta function, in which  $\mathbf{x}_f$  and  $\mathbf{x}$  are points at the interface and in the surrounding fluid, respectively. An indicator function  $I$ , which is unity and zero inside and outside the droplet, respectively, is defined to distinguish the droplet and surrounding fluid. The density and viscosity field can then be evaluated by the following equations:

$$\mu = \mu_0 + (k_\mu\mu_0 - \mu_0)I, \rho = \rho_0 + (k_\rho\rho_0 - \rho_0)I, \quad (3)$$

where  $\mu_0$  and  $\rho_0$  are the viscosity and density of the surrounding fluid, respectively, and  $k_\rho$  and  $k_\mu$  are the ratios of the viscosity and density of the droplet and the surrounding fluid. The indicator function  $I$  is obtained by solving the Poisson equation:

$$\nabla^2 I = \nabla \cdot \mathbf{G}, \quad (4)$$

where  $\mathbf{G}$  is the gradient of the indicator function  $I$  and restructured by the marker points information of the interface represented by the Lagrangian grid points:

$$\mathbf{G} = \nabla I = \int_A \mathbf{n}_f\delta(\mathbf{x} - \mathbf{x}_f)dA. \quad (5)$$

Here,  $\delta$  is a smoothed approximation of the Dirac Delta function, in the present three-dimensional study, which is a product of multiplying three one-dimensional delta functions as:

$$\delta(\mathbf{x} - \mathbf{x}_f) = \delta(x - x_f)\delta(y - y_f)\delta(z - z_f), \quad (6)$$

where a cosine functions proposed by Peskin [33] is chosen as the discretized form:

$$\delta(r) = \begin{cases} \frac{1}{4h}(1 + \cos(\frac{\pi r}{2h})) & \text{if } |r| \leq 2h, \\ 0 & \text{if } |r| > 2h, \end{cases} \quad (7)$$

where  $h$  is the uniform interval of the Eulerian mesh.

The motion of droplets on solid surfaces is governed by the flow of the surrounding fluid and the movement of the contact line, and thus physical modeling of the MCLs is essential. Generally, a stress singularity near the contact line due to the no-slip boundary condition requires special treatment. To this end, the classical NBC [34] for slip boundaries is widely used to determine the slip velocity at the contact line. However, in the NBC, an additional model is required to account for the influences of fluid–fluid interfacial forces. Accordingly, Qian et al. [8,32] developed the GNBC to further consider the effect of interfacial force on the MCL dynamics;

in this model, the slip velocity  $\mathbf{u}_{\text{slip}}$  on the solid surface is proportional to the viscous shear stress on the solid surface  $\tau^{\text{vis}}$  and the unbalanced Young's stress  $\tau^Y$ :

$$\beta'\mathbf{u}_{\text{slip}} = \tau^{\text{vis}} + \tau^Y. \quad (8)$$

Here,  $\beta'$  is a coefficient with the form  $\mu/\lambda$  ( $\lambda$  is the slip length defined as a vertical distance relative to the wall where the tangential velocity component vanishes). The unbalanced Young's stress can be derived using Young's relation, in which the surface tension of liquid–liquid interface and the contact angle are introduced. Note that, Qian et al. [32] reported that the GNBC is only valid for  $Ca_{\text{cl}} < 0.1$  (defined by the contact line speed). Besides, the Young's stress component is several orders of magnitude larger than the viscous component in the CL region, especially when the capillary number is relative small (in the order of  $10^{-2} \sim 10^{-1}$  in the present study). In this case, the viscous stress in the GNBC can be safely neglected.

### 3. Numerical method

#### 3.1. Front-tracking method

In the FT method, the flow is solved on a stationary Eulerian grid point, and the deformed fluid–fluid interface is tracked by a Lagrangian mesh. The Lagrangian mesh consists of a set of marker points moving with the local fluid velocity stored at the stationary Eulerian grid. The surface tension of the fluid–fluid interface can then be computed on the Lagrangian mesh and distributed onto the Eulerian mesh as a body force term in the momentum equations. In addition, the indicator function is calculated based on the interface location and is then used to update the fluid properties, i.e., viscosity and density.

To solve the flow field inside and outside the droplet, the governing equations are normalized with characteristic quantities, including length  $R$ , velocity  $\gamma R$ , and time  $\gamma^{-1}$ . Here,  $\gamma$  is the shear rate, and  $R = (0.75V/\pi)^{1/3}$  is the equivalent droplet radius, where  $V$  is the droplet volume. Non-dimensional numbers are summarized as follows:

$$Re = \frac{\rho_0\gamma R^2}{\mu_0}, Ca = \frac{\mu_0\gamma R}{\sigma}, k_\rho = \frac{\rho}{\rho_0}, k_\mu = \frac{\mu}{\mu_0}. \quad (9)$$

The three-stage RKCN four-step projection method proposed by Ni et al. [35] is employed to solve the Navier–Stokes equations, i.e., Eqs. (1) and (2) on a stationary collocated uniform Cartesian grid. The spatial derivatives are discretized using a second-order central difference scheme. The computational procedures from time level  $n$  to time level  $n + 1$  are briefly described as follows:

- (1) With a given velocity and pressure at time level  $n$ , the first predictor velocity is solved; a second-order Crank–Nicolson scheme is applied for the diffusion term to ensure numerical stability, and the convective term is updated using the third-order explicit Runge–Kutta technique.
- (2) The second predictor velocity is then obtained based on the first predictor velocity and the pressure gradient at time level  $n$ .
- (3) The intermediate velocity flux is interpolated from the second predictor velocity, based on which the pressure at time level  $n + 1$  is calculated by solving the pressure Poisson equation. Note that the pressure Poisson equation is solved using a V-cycle multigrid method [36] and the alternating direction implicit technique.
- (4) The velocity at time level  $n + 1$  is finally updated by the second predictor velocity and the pressure gradient at time level  $n + 1$ .

After the flow field is solved on the Eulerian grid points, the velocity  $\mathbf{u}_f$  of the Lagrangian point is interpolated from adjacent

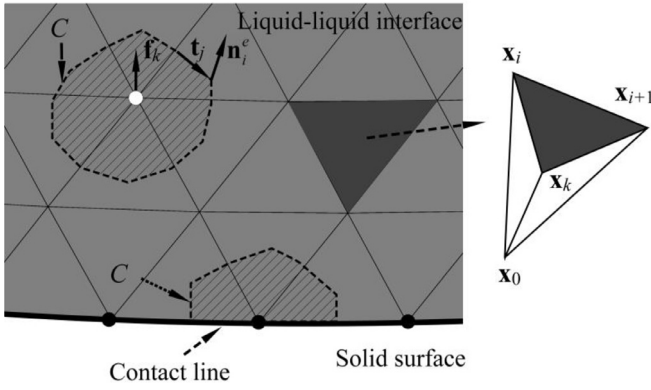


**Fig. 1.** Schematic illustration of the computational setup for surface tension (left) and local volume (right) at Lagrangian marker point  $\mathbf{x}_k$ , where the solid point and bold line are the contact line marker point and contact line, respectively, and  $C$  is the boundary of the surface segment.

Eulerian grid points as follows:

$$\mathbf{u}_f = \sum h_x h_y h_z \delta(\mathbf{x} - \mathbf{x}_f) \mathbf{u}, \quad (10)$$

where  $h_x$ ,  $h_y$  and  $h_z$  are uniform intervals of the Eulerian mesh along the  $x$ -,  $y$ - and  $z$ -axis, respectively. Based on the velocity interpolated from Eq. (10), the position  $\mathbf{x}_f$  of the marker point is updated using a second-order Adams-Basforth scheme as follows:

$$\mathbf{x}_f^{n+1} = \mathbf{x}_f^n + 0.5(3\mathbf{u}_f^{n+1} - \mathbf{u}_f^n)\Delta t, \quad (11)$$

where  $\Delta t$  is the time step size and the superscripts  $n+1$  and  $n$  represent the variables at the current and last time steps, respectively.

When the position of the Lagrangian marker points is updated at each time step, the volume of the droplet tends to decrease slightly, which may induce accumulated errors in long-term computations. In our method, the local and global volumes are both corrected at each time step. We employ the procedure reported by Li et al. [37] for the local volume correction. In this procedure, the local volume  $V_k$  for the  $k$ th Lagrangian point is defined as the volume of the polyhedron as shown in Fig. 1, which can be obtained as follows:

$$V_k = \frac{1}{6} \sum_{i=1}^{N_{\text{tri}}} [(\mathbf{x}_i - \mathbf{x}_0) \times (\mathbf{x}_{i+1} - \mathbf{x}_0) \cdot (\mathbf{x}_k - \mathbf{x}_0)]. \quad (12)$$

Here,  $\mathbf{x}_0$  is a reference point,  $N_{\text{tri}}$  is the number of triangular elements linked to the  $k$ th Lagrangian point, and  $\mathbf{x}_i$  and  $\mathbf{x}_{i+1}$  are the neighboring vertices of the  $i$ th element. A change in the local volume  $V_k$  may be induced as the position of the  $k$ th Lagrangian point is updated at time step  $n+1$ , and thus, the relative error of  $V_k$  can be computed as follows:

$$e_V(\mathbf{x}_k^{n+1}) = \frac{|V(\mathbf{x}_k^{n+1}) - V(\mathbf{x}_k^n)|}{V(\mathbf{x}_k^n)}. \quad (13)$$

Once  $e_V$  exceeds the prespecified tolerance  $tol$  ( $10^{-4}$  in this study), the updated position of the  $k$ th Lagrangian point is adjusted along the outward unit normal vector to ensure local volume conservation. Note that updating of the position and local volume correction is conducted alternately point after point. In addition, the conservation of the global volume of the droplet is also ensured by adjusting the position of each Lagrangian point along the direction from the center of the wetted area to the Lagrangian point. The relative volume loss  $|V - V_0|/V_0$  increases by 10% after 10,000 time steps, as shown in Fig. 2. In the present method, the value of  $|V - V_0|/V_0$  is of the order of  $10^{-5}$  and the computational time only increases by less than 1%.

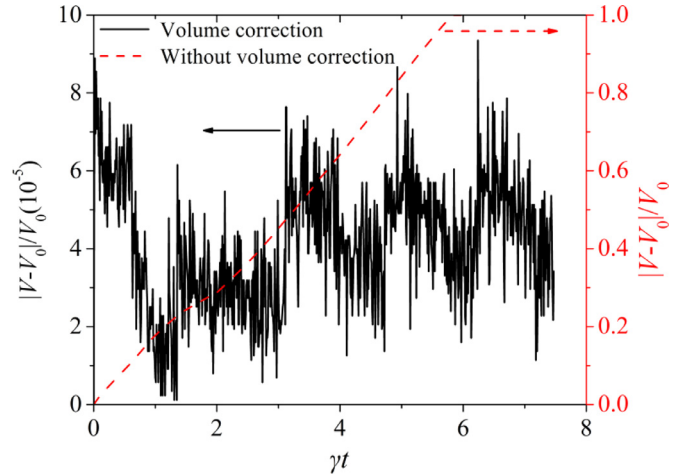


**Fig. 2.** Comparison of relative volume loss with the results without volume correction.

Based on the updated position of the interface, Eq. (5) is discretized as follows:

$$\mathbf{G} = \sum_k \delta(\mathbf{x} - \mathbf{x}_k^e) \mathbf{n}_k^e \Delta S_k, \quad (14)$$

where  $\mathbf{x}_k^e$ ,  $\mathbf{n}_k^e$  and  $\Delta S_k$  are the center position, unit outer normal vector and area of the  $k$ th triangular facet formed by linking the marker points. The successive over-relaxation method is used to solve the Poisson equation in Eq. (4). Then, the density and viscosity fields of the two-phase fluid are updated using Eq. (3).

We follow the procedure proposed by Esmaeeli and Tryggvason [38] to compute the surface tension. Generally, based on Stokes' theorem, the surface tension is converted to a contour integral over the edges of a surface segment instead of the surface integral of the curvature. Specifically, the quadrilateral surface segment consists of a third of all triangular elements connected to the  $k$ th Lagrangian point, in which the other three vertices contain two midpoints of the adjacent edges and the center point, as shown in Fig. 1. Accordingly, the surface tension term in the governing equation can be discretized as follows:

$$\begin{aligned} \int_A \sigma \kappa \mathbf{n}_f \delta(\mathbf{x} - \mathbf{x}_f) dA &= -\sigma \int_C \mathbf{t} \times \mathbf{n}_f \delta(\mathbf{x} - \mathbf{x}_k) dl \\ &\simeq -\sigma \sum \left( \delta(\mathbf{x} - \mathbf{x}_k) \sum_i^N \sum_{j=1}^2 \mathbf{t}_j \times \mathbf{n}_i^e \Delta l_j \right) \end{aligned} \quad (15)$$

Here,  $\mathbf{x}_k$  is the position of the  $k$ th Lagrangian point,  $\mathbf{n}_i^e$  is the outer unit vector of the  $i$ th element and  $\mathbf{t}_j$  and  $\Delta l_j$  are the unit direction vector and length of the  $j$ th edge, which is a segment of boundary  $C$ , as shown in Fig. 1. Note that the net force of three interfacial tensions acting on the contact line is considered as the boundary condition in the governing equations. Thus, the bounds of the integral in the right hand of Eq. (15) do not contain the contact line.

Since general procedures for the front-tracking/finite-difference method to model the dynamics of droplets freely suspended in flows are available in previous publications [29,30,39,40], our present paper only contains a brief description. In the following section, we emphasize additional treatments due to the presence of the MCL and the procedures to integrate the GNBC into the FT method.

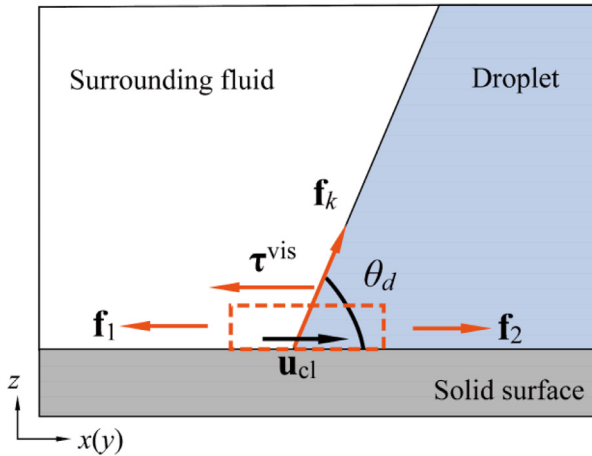


**Fig. 3.** Forces acting on the contact line, including the viscous stress and unbalanced Young's stress in the GNBC, where  $\mathbf{f}_1$  and  $\mathbf{f}_2$  are the two fluid-solid interfacial tensions. The dashed line represents the thin liquid layer adjacent to the contact line.

### 3.2. Integration of the generalized Navier boundary condition (GNBC) in the front-tracking (FT) method

The unbalanced Young's stress in the GNBC is derived from the average force acting on the molecules within a very thin layer adjacent to the wall. In the present work, this boundary condition is applied on the grid points of first layer near the wall. In particular, we employ the GNBC to calculate the slip velocity of the MCL and use this velocity as the boundary condition for solving the Navier-Stokes equations Eqs. (1) and ((2)). According to Eq. (8), the unbalanced Young's stress and viscous stress at the contact line must be computed first. In our FT method, the interfacial force acting on the contact line (i.e., the non-zero net force of the surface tension at the three interfaces connected to the contact line, as shown in Fig. 3) is computed and then converted to a stress distribution on the adjacent Eulerian grid points of the solid surface. Thus, the boundary conditions for the velocity (i.e., slip velocity) on the solid surface can be expressed as follows:

$$\begin{aligned} \mathbf{u}_{\text{slip}} = & \lambda \frac{\partial \mathbf{u}}{\partial z} \Big|_{\text{wall}} + \frac{\lambda \tau^Y}{\mu} = \lambda \frac{\partial \mathbf{u}}{\partial z} \Big|_{\text{wall}} \\ & + \frac{\lambda}{\mu} \sum \delta(x - x_k) \delta(y - y_k) \mathbf{f}_k (\cos \theta_e - \cos \theta_d). \end{aligned} \quad (16)$$

Here,  $\theta_d$  and  $\theta_e$  are the dynamic and equilibrium contact angles, respectively,  $\mathbf{f}_k$  is the surface tension computed according to Eq. (15) at contact line marker point  $\mathbf{x}_k(x_k, y_k, 0)$ , as seen in Fig. 3, in which a line integral is obtained only along the contact line. Note that the viscous stress term of the GNBC in Eq. (8) is ignored in our present study. The unbalanced Young's stress near the contact line is several orders of magnitude larger than the viscous stress when the capillary number based on the contact line speed (i.e., the speed computed at  $\mathbf{x} = \mathbf{x}_k$  according to Eq. (16))  $Ca_{\text{cl}} = \mu_0 u_{\text{cl}} / \sigma$  is less than 0.1 [32,41]. In our following simulations,  $Ca_{\text{cl}}$  is generally in the order of  $10^{-2}$  to  $10^{-1}$ .

In the GNBC, the microscopic contact angle characterized at the molecular scale is employed and is generally considered experimentally inaccessible. The macroscopic contact angle characterized at the length scale  $R$  in our FT method differs from the microscopic contact angle because the liquid–liquid interface near the contact line is generally a meniscus shape. Hence, the formulation introduced by Cox [42,43] is applied to relate the macroscopic and microscopic contact angles. The procedure to calculate the contact angle is presented in detail in Fig. 4. The contact line is discretized

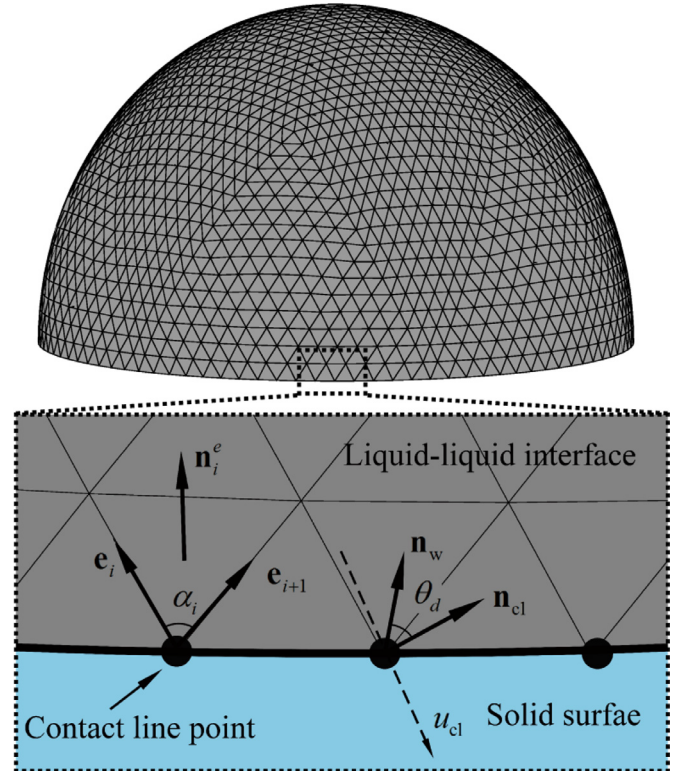


**Fig. 4.** Schematic illustration of the computational setup for the normal vector and the contact angle, where  $\alpha_i$  is the angle between the two vectors  $\mathbf{e}_i$  and  $\mathbf{e}_{i+1}$ ,  $\mathbf{n}_w$  is the unit outer normal vector of the solid surface, and  $\mathbf{n}_{\text{cl}}$  is the unit outer normal vector at the contact line marker point.

into a set of line segments, which are the edges of the triangular elements in contact with the solid surface. In our method,  $\theta_d$  is computed at each marker point of the contact line instead of at the center point of each line segment [44]. The unit outer normal vector of the liquid–liquid interface  $\mathbf{n}_{\text{cl}}$  at each contact line marker point is calculated as the weighted sum of normal vectors of all adjacent triangular elements as follows:

$$\mathbf{n}_{\text{cl}} = \sum_{i=1}^N \frac{\mathbf{n}_i^e \sin \alpha_i}{|\mathbf{e}_i||\mathbf{e}_{i+1}|} / \left| \sum_{i=1}^N \frac{\mathbf{n}_i^e \sin \alpha_i}{|\mathbf{e}_i||\mathbf{e}_{i+1}|} \right|. \quad (17)$$

Here,  $\alpha_i$  is the angle between the two vectors  $\mathbf{e}_i$  and  $\mathbf{e}_{i+1}$ , as shown in Fig. 4.  $\theta_d$  at the contact line marker point is represented as:

$$\theta_d = \arccos \left( \frac{\mathbf{n}_w \cdot \mathbf{n}_{\text{cl}}}{|\mathbf{n}_w||\mathbf{n}_{\text{cl}}|} \right), \quad (18)$$

where  $\mathbf{n}_w$  is the unit outer normal vector of the solid surface.

The motion of a droplet on a solid surface is significantly affected by contact angle hysteresis, which is characterized by the advancing contact angle  $\theta_A$  and the receding contact angle  $\theta_R$ . When the dynamic contact angle  $\theta_d$  exceeds the hysteresis window, the unbalanced Young's stress tends to reshape the droplet interface to its equilibrium shape (i.e.,  $\theta_d$  trends to reach the equilibrium contact angle  $\theta_A$  or  $\theta_R$ ), and the contact line will move, causing the droplet to slide on the solid surface. Thus, the slip velocity on the solid surface is determined based on the transformation in Eq. (16) without considering the viscous stress as follows:

$$\mathbf{u}_{\text{slip}} = \begin{cases} \frac{\lambda}{\mu} \sum_k \delta(x - x_k) \delta(y - y_k) \mathbf{f}_k (\cos \theta_R - \cos \theta_d) & \text{if } \theta_d < \theta_R, \\ 0 & \text{if } \theta_R \leq \theta_d \leq \theta_A \\ \frac{\lambda}{\mu} \sum_k \delta(x - x_k) \delta(y - y_k) \mathbf{f}_k (\cos \theta_A - \cos \theta_d) & \text{if } \theta_d > \theta_A. \end{cases} \quad (19)$$

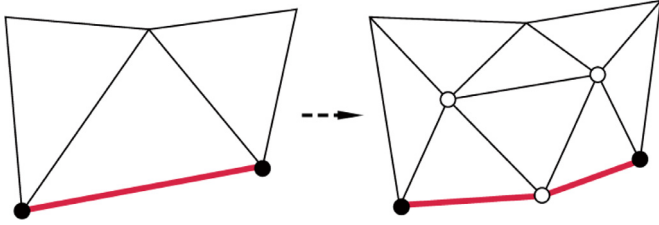


**Fig. 5.** Illustration of edge splitting of the contact line element (i.e., the bold line), where the solid points are contact line marker points. Three new marker points (i.e., empty points) and five new elements are generated.

Note that the static contact angle  $\theta_e$  without considering the hysteresis can also be variable for a practical solid surface, e.g., a constant wettability gradient [45,46] or an alternating-stripe-patterned wettability [47,48].

### 3.3. Lagrangian mesh restructuring

The droplet interface may present large deformation due to the flow of the surrounding fluid, which results in the stretching and shrinking of the Lagrangian mesh. Therefore, the Lagrangian mesh must be optimized to maintain its high quality. Previously developed mesh optimization techniques include (1) inserting/deleting vertices [49], (2) swapping edges/faces [50], and (3) moving vertices without changing the mesh topology [51]. In our model, the first and third techniques are employed.

To insert/delete vertices, we follow the same procedure proposed by Tryggvason et al. [39] for the general FT method without considering the contact line. Two parameters are used to control the quality of the mesh including the length of the edge and the shape of the triangle. Here, we emphasize the special treatments required for linking the Lagrangian mesh with the contact line to ensure the accurate computation of the unbalanced Young's force (Eq. (16)). The premise is to properly preserve the interface features near the contact line during the processes of edge insertion/deletion, and hence, the interface must be accurately represented using a sufficient number of Lagrangian marker points near the contact line. The edge consisting of the contact line marker points is split, as shown in Fig. 5; in this case, the number of adjacent points for each contact line marker point is larger than 3. Fig. 6 shows the cases that may arise for the edge collapse of the Lagrangian mesh near the contact line. The edge collapsing procedure is strictly conducted to avoid generating unacceptable mesh, such as causing a mesh triangle to fold over another or create a non-manifold triangulation. In addition, a fifth-order polynomial interpolation is used to readjust the positions of the contact line markers after the contact line element is split or collapsed. For our simulations, all procedures described above are applied on the Lagrangian mesh 5 times at intervals of 50 time steps.

For a spherical droplet initially resting on a solid surface with a uniform contact angle  $\theta_0$ , we calculate the contact angle at each contact line marker point. The value is essentially not influenced by the edge splitting/collapsing procedure, and the maximum error is only  $5 \times 10^{-3} \pi$  for contact angles varying from 0 to  $\pi$ . Fig. 7 displays the maximum error  $e_m$  and the  $l_2$ -norm error after edge splitting/collapsing.  $e_m$  is as low as 1% for a wide range of contact angles, and  $e_m$  is maintained within 1.5% for all simulations. In addition, we obtained the same conclusion for the computation of surface tension. Overall, the computational contact angle and surface tension are essentially not influenced by the implementation of edge splitting/collapsing of the Lagrangian mesh near the contact line.

The edge splitting/collapsing procedure maintains the size and shape of the triangular mesh in an acceptable range. The mesh

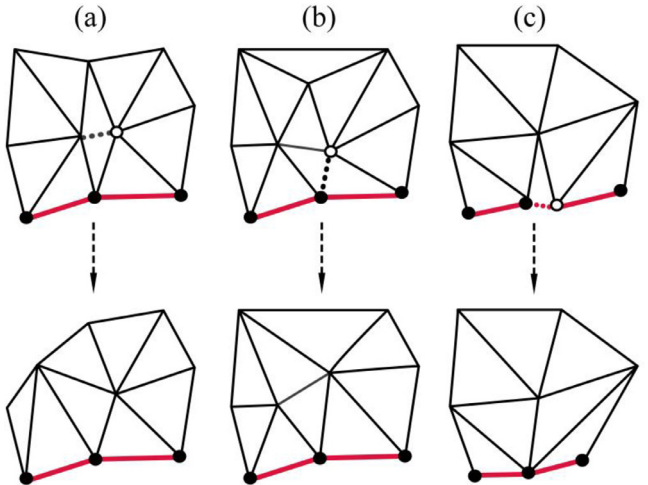


**Fig. 6.** Sketch of edge collapsing of the Lagrangian mesh in contact with the contact line (i.e., the bold line), where the dashed lines represent the edges to be collapsed, which are classified into three categories: (a) the edge is opposite a contact line marker point (i.e., solid point), (b) one vertex of the edge is a contact line marker point, and (c) the edge consists of two contact line marker points. The empty point represents the Lagrangian marker point to be removed. Note that edge collapse is avoided when the number of Lagrangian points in contact with the contact line marker point is less than five.

quality can be enhanced by narrowing the limits of the control parameters. However, the improvement is still very limited and may create additional problems such as an infinite loop for edge splitting. In the present paper, the feature-preserving suboptimal Delaunay triangulation (S-ODT) is applied to improve the Lagrangian mesh quality as well as to preserve the curvature feature on the original mesh. All Lagrangian marker points are readjusted in each iteration according to their categories, which are distinguished by the curvature in the neighborhood using the local structure tensor [52]. The process is repeated until the mesh quality meets some predefined criteria or a maximum number of iterations is reached. A detailed description of the feature-preserving S-ODT algorithm can be found in Refs. [52,53]. The application frequency is dependent on the problem, the mesh resolution, and the time step. In our simulations, this procedure is applied on the Lagrangian mesh 5 times at intervals of 100 time steps. The computational time only increases by approximately 4%.

Two parameters are defined to represent the quality of the Lagrangian mesh, i.e., the angle  $\theta_{tri}$  and the shape parameter  $sp$  of the triangular mesh, where  $\theta_{tri}$  is the interior angle of the triangular mesh, and  $sp$  is defined as twice the ratio of the radii of the inscribed and circumscribed circles of the triangular mesh. Fig. 8 shows the results of the angle and sharp histograms before and after the feature-preserving S-ODT, which reveal that the quality of the Lagrangian mesh is significantly improved and the number of low-quality grid points is significantly reduced compared with the results using the initial mesh without any interface operations. Two statistical errors  $e_n(\theta_{tri})$  and  $e_n(sp)$  are defined to represent the distribution of the mesh quality. The improved mesh quality is significantly maintained as the interface deforms under flow, as shown in Fig. 8. Furthermore, we also found that the number of Lagrangian grid points (i.e.,  $N_e$ ) is significantly decreased in case of a high-quality Lagrangian mesh. This indicates that the feature-preserving S-ODT is capable of effectively reducing the computational cost to optimize the Lagrangian mesh.

We compared the deformation of a droplet under shear flow under three different mesh schemes: (a) initial mesh without any interface treatments, (b) applying edge splitting/collapsing, and (c) applying edge splitting/collapsing and the feature-preserving S-

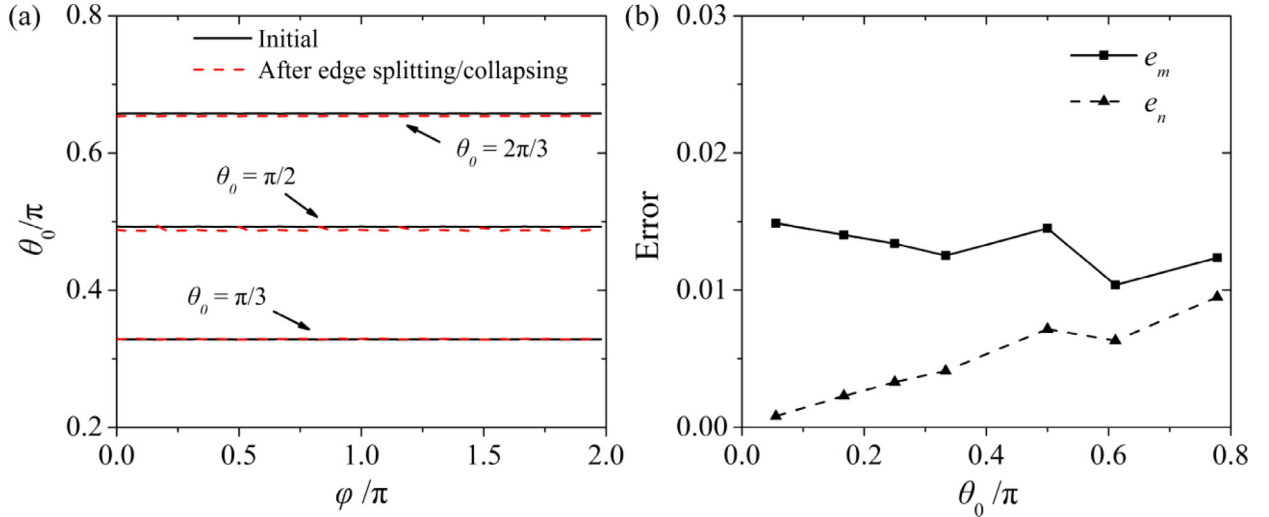


**Fig. 7.** Left: the computed contact angles before and after edge splitting/collapsing for  $\theta_0 = \pi/3, \pi/2$  and  $2\pi/3$ . Right: The maximum relative error  $e_m = \max\{|\theta_{0i} - \theta_0|/\theta_0\}$  and discrete  $l_2$ -norm error  $e_n = \sqrt{\sum_{i=1}^{N_{cl}} |\theta_{0i} - \theta_0|^2 / N_{cl}}$  after edge splitting/collapsing, where  $N_{cl}$  is the number of contact line marker points.

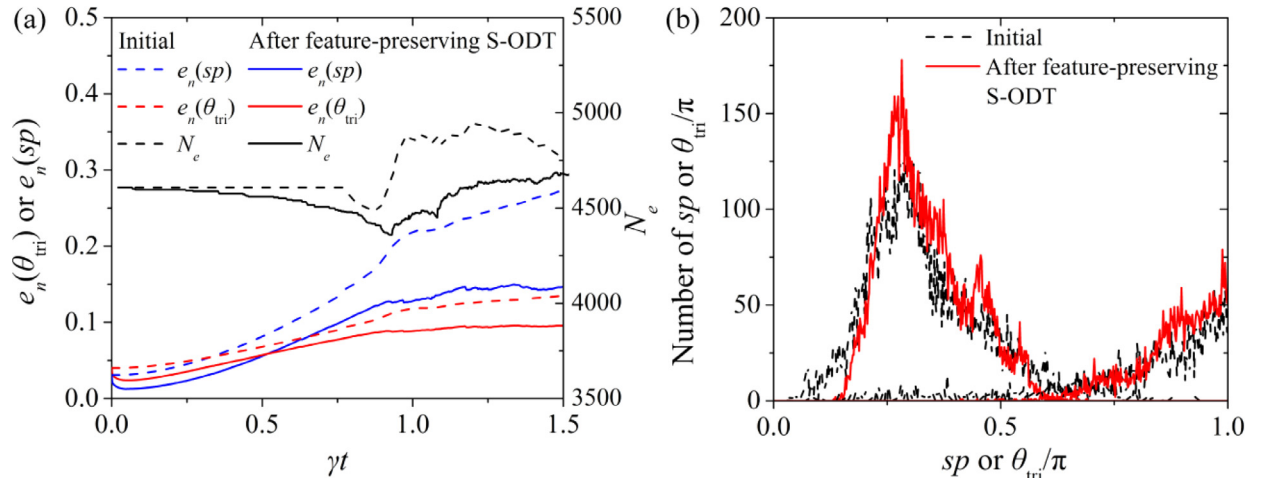


**Fig. 8.** Effect of the feature-preserving S-ODT on the quality of the Lagrangian mesh, i.e.,  $sp$ ,  $\theta_{\text{tri}}$  and  $N_e$ . Left: The evolution of  $e_n(\theta_{\text{tri}}) = \sqrt{\sum_{j=1}^{N_1} |\theta_{\text{trj}} - \pi/3|^2 / N_1}$ ,  $e_n(sp) = \sqrt{\sum_{i=1}^{N_e} |sp_i - 1|^2 / N_e}$  and  $N_e$  during interface deformation, where  $N_1 = 3N_e$ . Right: The shape  $sp$  and angle  $\theta_{\text{tri}}$  histograms of the Lagrangian mesh for the deformed interface.

ODT. The deformation parameter  $D = (L - B)/(L + B)$  is defined to quantify the droplet shape, where  $L$  and  $B$  are the maximum and minimum distance from the interface to the center of the wetted area enclosed by the contact line, respectively. As shown in Fig. 9, the simulation results show no significant differences between these three cases in the beginning stages of deformation. However, after the interface deforms more significantly by neglecting the inertial effect, the solution for the case without applying any interface optimizations unexpectedly diverges. Simultaneously, the deformation of the droplet continues oscillating for the case in which the edge splitting/collapsing technique is only applied for the Lagrangian mesh. The simulations show that optimizing the Lagrangian mesh guarantees the stability of the interface reconstruction itself and enhances the overall computational stability. This is also apparent by examining the quality of the Lagrangian mesh, as shown in Fig. 9, by the angle and shape histograms for the Lagrangian mesh at  $\gamma t = 4$ . These results confirm that the feature-preserving S-ODT, in addition to edge splitting/collapsing, is an indispensable procedure. Moreover, the accumulated error associated with the optimization procedure is negligible since the interface grid points are well distributed during the entire simulation. After

reconstructing, the velocities of each Lagrangian point on the interface are all interpolated from adjacent Eulerian grid points again.

### 3.4. Material indicator function near the contact line

When the interface touches a solid surface, to provide a reasonable dynamic description of the MCL using the GNBC, an accurate solution of the material field (i.e., viscosity) near the contact line is required, which is constructed from the known position of the interface. For the solution of Poisson equation in Eq. (4), in addition to the high-quality of Lagrangian mesh, the boundary conditions for the indicator function  $I$  must be prescribed on the touched wall. We cannot simply prescribe values of  $I$  with explicit Dirichlet boundary conditions, e.g., simple values of one or zero, as this may result in an abrupt jump in the material parameters. Khener [54] uses a linear iteration method to ensure that the contour curves of the indicator function adjacent to the interface are smooth and intersect the wall at the required contact angle. However, to calculate the correct transition of the indicator function across a solid surface, a few iterations are generally required. Based on the idea that the indicator function has characteristics of

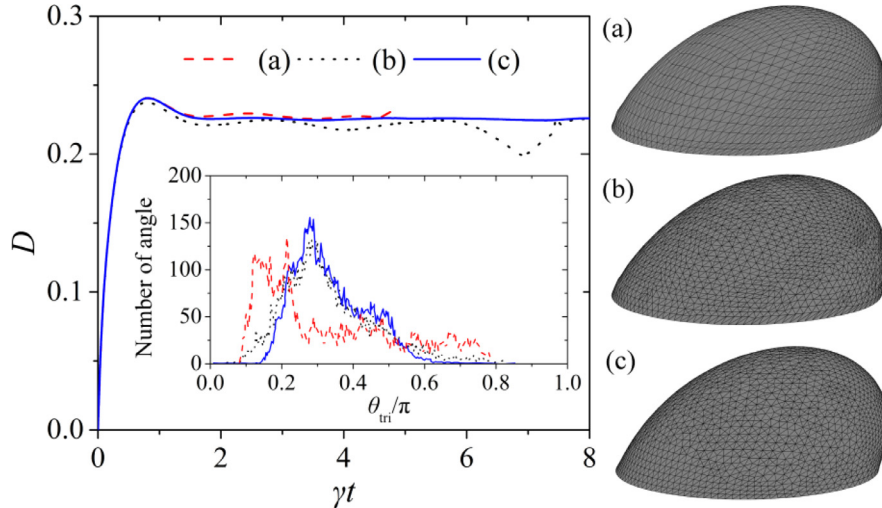


**Fig. 9.** Evolutions of droplet deformation (a) without any interface operations, (b) with mesh restructuring, and (c) with mesh restructuring and the feature-preserving S-ODT. The inset shows the angle and shape histograms for the Lagrangian mesh at  $\gamma t = 4$ .

a Heaviside function, which can also be found by using the distance function as in the level-set method, we developed a new procedure for computing  $I$  from the existing interface to assign the boundary values of  $\mathbf{G}$  with explicit Neumann conditions. Here, we briefly describe the basic idea. For a given Lagrangian mesh, the unit normal vector of the interface is converted to a vector field distribution  $\mathbf{n}$  onto the adjacent Eulerian grid points:

$$\mathbf{n} = \sum_k D(\mathbf{x} - \mathbf{x}_k) \mathbf{n}_k. \quad (20)$$

Thus, the direction of  $\mathbf{G}$  is opposite the local outer vector normal to the closest interface. The projection of  $\mathbf{G}$  into the solid surface, i.e.,  $G_x$  and  $G_y$ , can be determined by solving the equation on the two-dimensional surface (i.e., the surface at  $\mathbf{x} = \mathbf{x}_w$ ) using the existing contact line markers as follows:

$$\mathbf{G}|_{\mathbf{x}=\mathbf{x}_w} = \sum D(\mathbf{x}_w - \mathbf{x}_{\text{cl}}) \mathbf{n}_{\text{cl}}, \quad (21)$$

where  $\mathbf{x}_{\text{cl}}$  and  $\mathbf{n}_{\text{cl}}$  are the middle position and the unit outer normal vector of the contact line element and  $\mathbf{x}_w$  is the coordinate of the Eulerian mesh on the solid surface. By combining Eqs. (20) and (21), the perpendicular component  $G_z$  near the contact line can be calculated using the vector field  $\mathbf{n}(n_x, n_y, n_z)$  as follows:

$$\frac{\sqrt{G_x^2 + G_y^2}}{G_z} = -\frac{\sqrt{n_x^2 + n_y^2}}{n_z}. \quad (22)$$

$\mathbf{G}(G_x, G_y, G_z)$  is updated at each time step and then is imposed as the boundary condition to solve Eq. (14). Thus, the exact solution of the material fields can be updated according to Eq. (3).

The indicator function calculated from the above procedure near the contact line is shown in Fig. 10. This approach gives good results for the material field, and a smooth transition of the indicator function across the interface is observed. The contour curve of  $I$  inserts into the solid surface at the approximate contact angles, which are prescribed as  $\pi/3$ ,  $\pi/2$  and  $2\pi/3$ , especially where the contour curve remains sufficiently close to the interface. With this approach, the accuracy of the material field near the contact line can be guaranteed when the contact line moves, as long as a high-quality Lagrangian mesh is present and the calculations of vectors normal to the interface are accurate. Fortunately, all these requirements are achieved by implementing the edge splitting/collapsing and feature-preserving S-ODT procedures described above. Besides, the approach proposed in the present paper can also be applied in other methods to calculate the material field near the contact line.

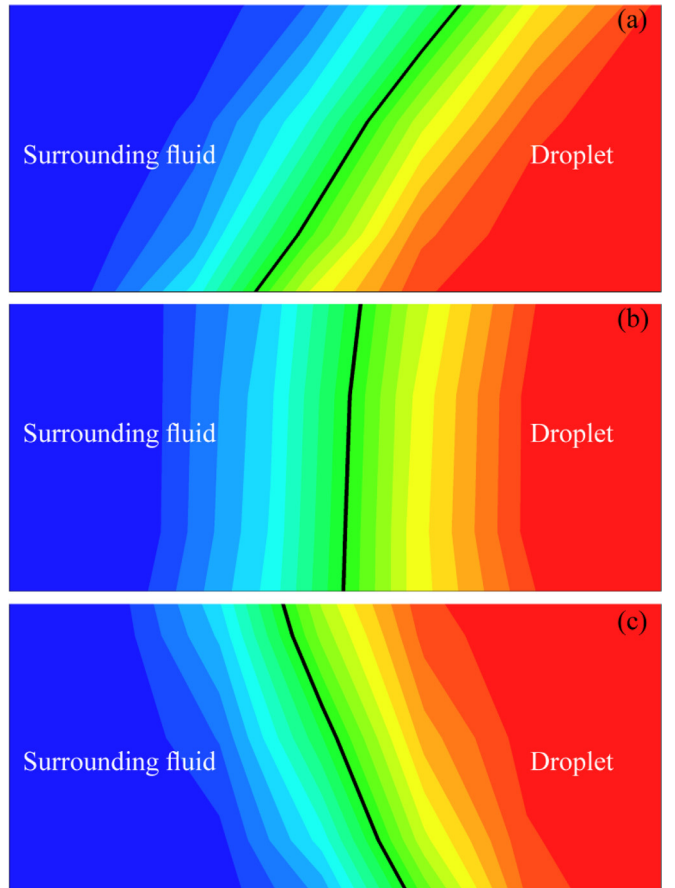


**Fig. 10.** The contour curves of indicator function  $I$  near the contact line for  $\theta_0 = \pi/3$  (upper),  $\pi/2$  (middle) and  $2\pi/3$  (bottom), where the black solid lines are the interface represented by the contour curve  $I = 0.5$ .

#### 4. Validation and results

A number of tests were performed to validate our numerical method and to assess its robustness and precision. First, we present some numerical results of a sessile droplet to validate the surface tension computation. Secondly, a droplet adhering to a wall with fixed contact lines is studied and the result is compared with the theoretical and numerical solutions. Then, the spreading of the

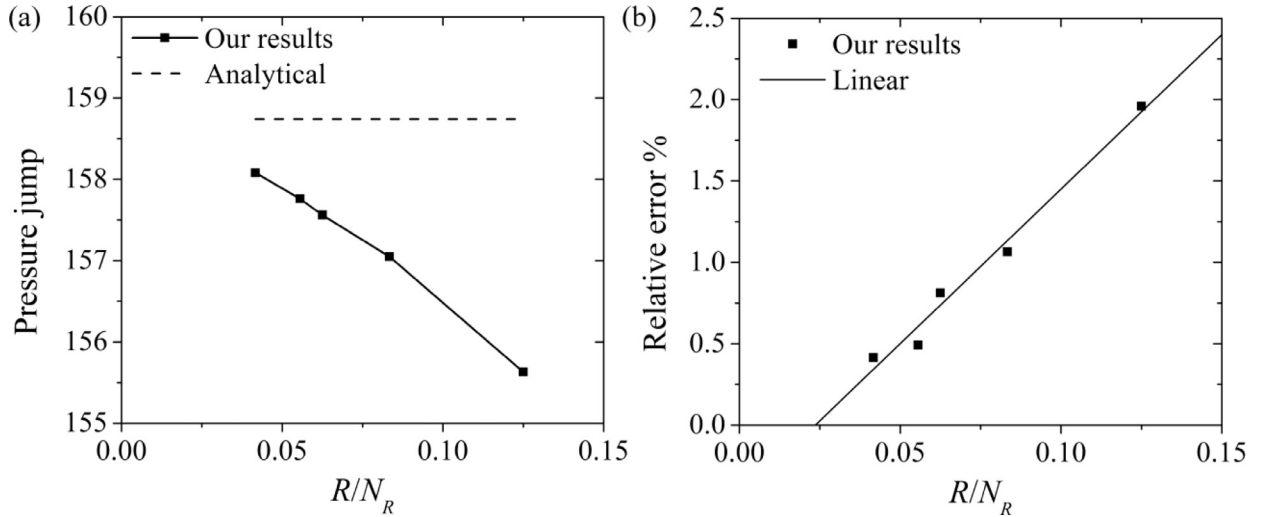


**Fig. 11.** Our numerical pressure jump is close to the analytical pressure jump (left) given by the Young–Laplace equation and its relative error (right) is presented for different numbers  $N_R$  of Eulerian grid points.

droplet and the motion of the droplet under a shear flow with MCLs are considered. Finally, the influence of hysteresis in the GNBC on the motion of the droplet is investigated to illustrate the capability of our method.

#### 4.1. Sessile droplet

A stationary hemispherical droplet was placed on the center of a solid surface under quiescent flow. The surface tension tends to induce a spherical droplet in the absence of viscous, gravitational, or external forces. The pressure jump across the spherical interface is given by the following equation based on the Young–Laplace equation [55]:

$$\Delta p = \frac{2\sigma}{R_0}, \quad (23)$$

where  $R_0$  is the initial radius of the droplet. In the present work, because all length parameters are normalized with the equivalent radius  $R$ , the parameter  $\Delta p$  can be written as follows:

$$\Delta p = \frac{2\sigma}{\sqrt[3]{2}R}. \quad (24)$$

The density and viscosity of the droplet are equal to the continuous phase. The interface tension coefficient is  $\sigma = 10^{-2}$  N/m, and the equivalent radius  $R$  of the droplet is  $10^{-4}$  m. In this case, the analytic value of the pressure jump at the interface is  $158.74$  N/m<sup>2</sup>. Numerical simulations were performed for five different uniform mesh,  $N_R = 8, 12, 16, 18$ , and  $24$ , and the pressure difference across the fluid interface  $[\rho] = p_{\max} - p_{\min}$  was plotted, where  $p_{\max}$  and  $p_{\min}$  are the maximum and minimum pressure inside and outside the droplet, respectively. Fig. 11 shows that the numerical pressure jump as a result of surface tension force approaches to the analytic value given by the Young–Laplace equation. These numerical results are accurate with a relative error of less than 1.8% for the coarsest mesh, which is reduced to approximately 0.4% when the mesh is refined.

As stated by Tryggvason et al. [39], any significant anisotropy of the surface tensions on the Lagrangian mesh can cause small unphysical velocities near the interface, i.e., parasitic currents. These unphysical velocities depend strongly on many factors such as mesh resolution, viscosity, surface tension, etc. A hemispherical static droplet rested on a solid surface and immersed in a continuous stationary phase is simulated without considering gravity. The capillary-viscous length  $R_v = 0.001$  is used in the problem,

where  $R_v = \rho v^2/\sigma$ ,  $v$  is the kinematic viscosity. The maximum spurious velocities  $u_{\max}$  for droplet with different numbers  $N_R$  of Eulerian grid points is plotted versus time in Fig. 12(a). A maximum spurious velocity of  $O(10^{-2})$  is obtained with  $N_R = 8$ . For the fine gird with  $N_R = 18$ , we obtained a maximum spurious velocity of  $O(10^{-3})$ . Fig. 12(b) and (c) displays the vector and contour of velocities caused by the small fluctuations near the interface after 1000 time steps (i.e.,  $\gamma t = 0.1$ ). These results show that the parasitic currents generated by our code are quite small, and do not degrade the solutions when the surface tension coefficient is high.

#### 4.2. Droplet subjected to a shear flow with fixed contact lines

Droplets adhering to solid surfaces have long been studied because they are not only commonly observed in nature and engineering applications but also involve complex flow phenomena, such as contact line pinning, detachment, and breakup from the solid surface. All these behaviors are related to the deformation of droplets adhered to a solid surface. We consider the droplet initially placed on the solid surface and subsequently deforming in a shear flow, in which the effect of upper confining wall is ignored. The viscosity and density of the droplet are taken to be equal to those of the surrounding fluid ( $k_\mu = 1$  and  $k_\rho = 1$ ).

First, the numerical simulations were performed for five different uniform meshes, with  $N_R = 8, 12, 18, 24$ , and  $28$ . Fig. 13 displays the deformation parameter  $D$  converging to the value computed at the finest mesh, and the error as the mesh is refined. These numerical results are accurate with a relative error of less than 1.1% for the coarsest mesh, i.e.,  $N_R = 8$ , which is reduced to approximately 0.2% for the mesh resolution (i.e.,  $N_R = 18$ ) used in the present paper.

We compared our results with the analytical solution [56] and numerical simulation [57,58] when inertia effects are neglected. The capillary number  $Ca$  varies from 0 to 0.15. The initial contact angle  $\theta_0$  is  $\pi/2$ . Fig. 14 displays the instantaneous shape for an adherent droplet with  $\theta_0 = \pi/2$  in a simple shear flow at  $Ca = 0.15$ . The numerical results were compared with the results of the simulation using the three-dimensional boundary element method of Dimitrakopoulos [58]. The time evolutions of the interfacial profile indicate that our method achieves very good performance. The deformation parameter  $D$  and the contact angles  $\theta_{\text{up}}$  and  $\theta_{\text{down}}$  at steady state are plotted as a function of the capillary number in Fig. 15, where  $\theta_{\text{up}}$  and  $\theta_{\text{down}}$  are the contact angles at the end

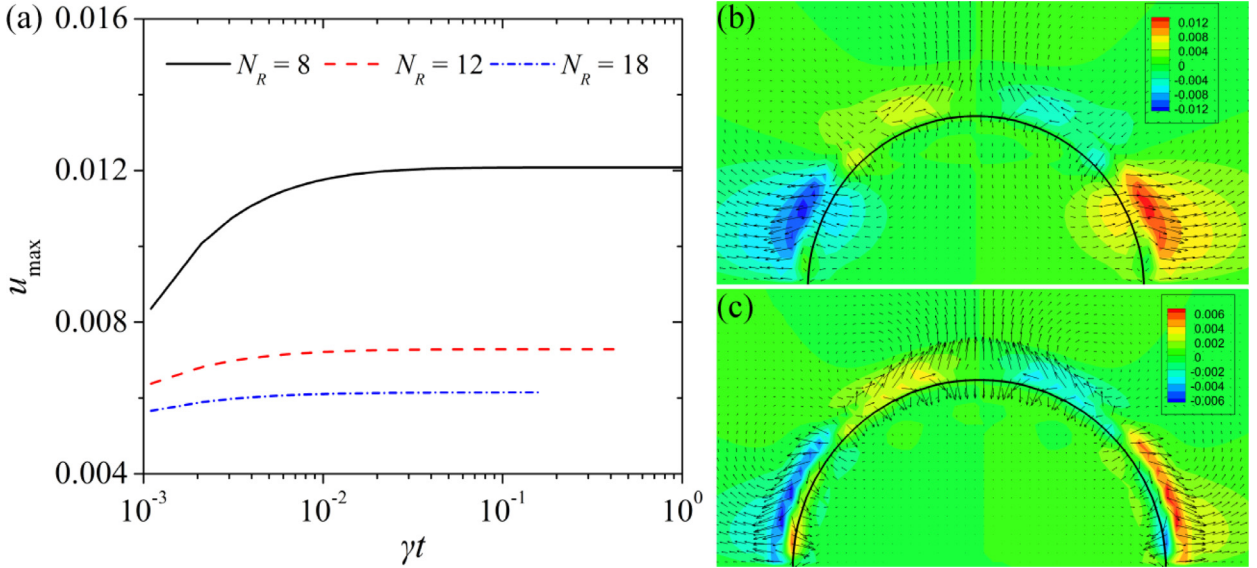


**Fig. 12.** (a) Maximum spurious velocities for droplet for different numbers  $N_R$  of Eulerian grid points. (b) and (c) Velocity contour and velocity vectors for  $N_R = 8$  and  $N_R = 18$  for  $R_v = 0.001$ , respectively, where solid lines represent the droplet interface.

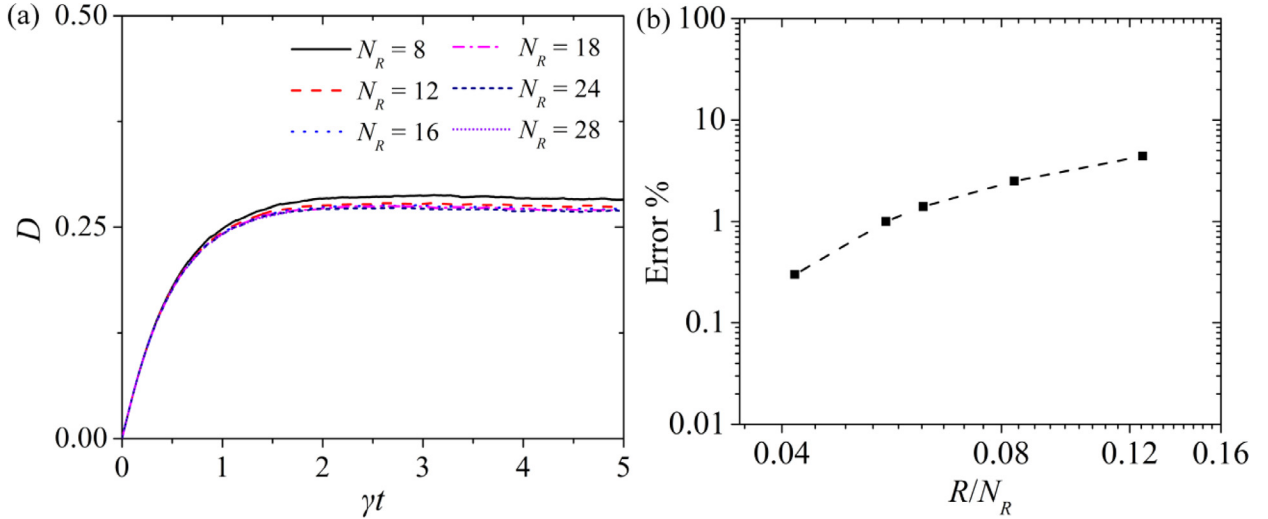


**Fig. 13.** Numerical performance tests by simulating deformation of a droplet with fixed contact line for varying Eulerian resolution.  $N_R$  is the number of Eulerian grid points for one radius of the droplet.

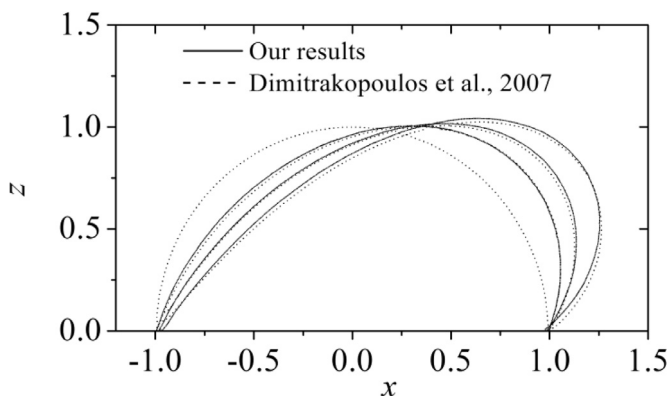


**Fig. 14.** Deformation of an adherent droplet with  $\theta_0 = \pi/2$  in simple shear flow with  $Ca = 0.15$ . Here, the instantaneous droplet profile is tracked at  $t = 0, 0.5, 1$ , and  $10$ . The dashed line is the droplet shape tracked using the three-dimensional boundary element method of Dimitrakopoulos [58].

of the upstream and downstream contact lines. In Dimitrakopoulos's work, [58] only a given shape of the droplet is obtained. The results obtained by our method are in good agreement with the previous results. Both  $\theta_{\text{up}}$  and  $\theta_{\text{down}}$  have approximately linear relationships with  $Ca$  at steady state.

#### 4.3. Droplet spreading under gravity

The effect of gravity on droplet spreading on a solid surface was studied in this section. The droplet was initially part of a sphere spread on a horizontal solid surface. In the present section, the differences in density and viscosity inside and outside the droplet are considered. The viscosity and density ratio are thus  $k_\rho = 10$  and  $k_\rho = 10$ . The computational domain size  $L_x \times L_y \times L_z$  is  $8R \times 8R \times 5R$ , and the droplet is placed at the center of XY-plane. The initial contact angle  $\theta_0$  is equal to  $\theta_e$ . The droplet deforms due to gravity, and the contact line moves to reach  $\theta_e$ . The final shape of the droplet is related to the Eotvos number  $Eo = k_\rho \rho_0 g R^2 / \sigma$  and

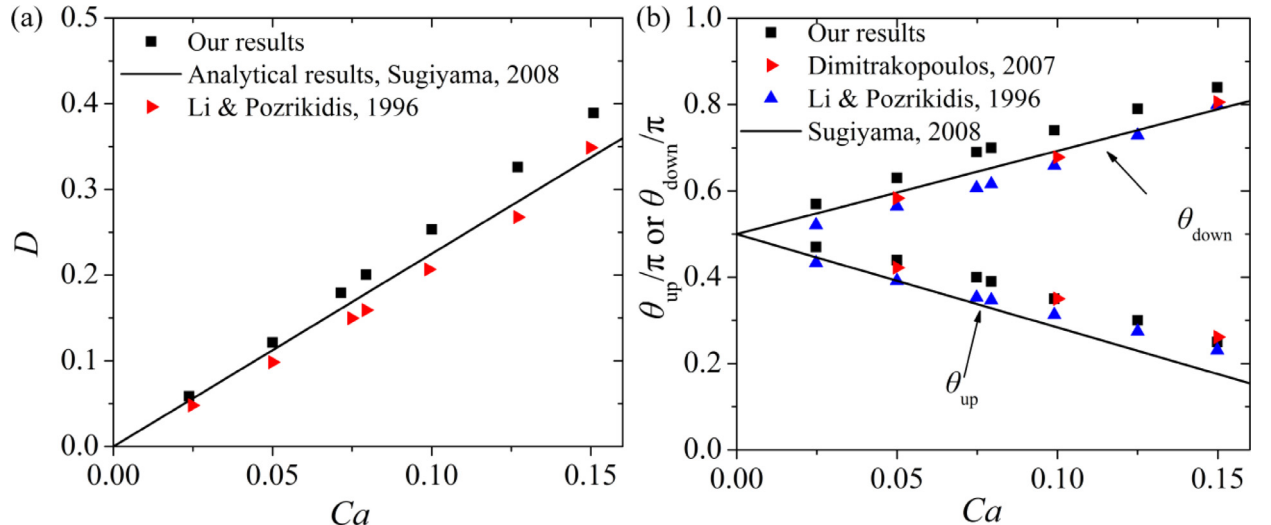


**Fig. 15.** The variations of the steady-state deformation (left) and contact angle (right) for different capillary numbers.

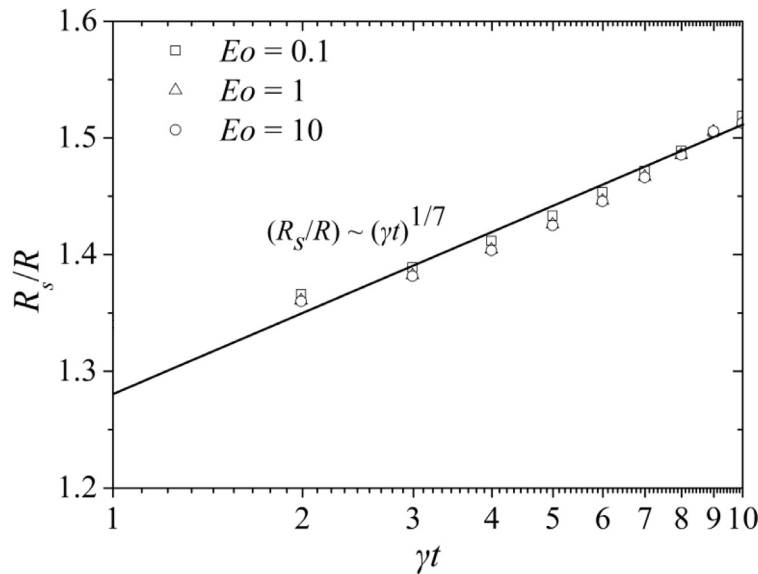


**Fig. 16.** The spreading radius  $R_s$  of the droplet as a function of time with different Eotvos numbers. The solid line is described by Ehrhard and Davis [59], where the driving force is gravity and the dissipation occurs only at the contact line.

$\theta_e$  [26].  $h_d$  is defined as the maximum vertical distance between the droplet and the solid surface.

The evolution of the spreading radius  $R_s$  is obtained for different Eotvos numbers by our simulation as shown in Fig. 16. As stated by Ehrhard and Davis [59], if the droplet changes towards a “pancake” shape driven by the gravity, the driving force was balanced against dissipation at the contact line. In this case, a scaling law with  $R_s \sim t^{1/7}$  is in a good agreement with that of ours.

For  $Eo \leq 1$ , the state-steady height  $h_d$  of the droplet is controlled by the surface tension and  $\theta_e$ . Then,  $h_d$  is calculated as follows:

$$h_d = R_0(1 - \cos\theta_e)\sqrt{\frac{\pi}{2(\theta_e - \sin\theta_e \cos\theta_e)}}, \quad (25)$$

where  $R_0$  is the initial radius of the droplet, as shown in Fig. 17. For  $Eo \geq 1$ ,  $h_d$  is directly proportional to the capillary length:

$$h_d \rightarrow 2\sqrt{\frac{\sigma}{k_p \rho_0 g}} \sin\left(\frac{\theta_e}{2}\right) = \frac{2R}{\sqrt{Eo}} \sin\left(\frac{\theta_e}{2}\right). \quad (26)$$

In this case,  $h_d$  is computed for Eotvos numbers varying from 0.1 to 10. The variation of  $h^*$  is plotted versus the Eotvos number in Fig. 17, where  $h^*$  is the normalized height defined as  $h_d/R$ . The simulations are in very good agreement with the two solutions calculated by Eqs. (25) and (26).

#### 4.4. Droplet subjected to a shear flow with MCLs

In our method, the behavior of the contact line is completely described by the GNBC, and the mesh independence of the GNBC was first tested. The relationship between  $Ca_{cl}$  and  $\theta_d$  is mutually independent of the Lagrangian mesh size  $N_t$  (the initial number of the triangular mesh for the fluid interface). The convergence of the method for the GNBC calculation is shown in Fig. 18. For a constant slip length, as shown in Eq. (16), the contact line speed depends exclusively on the unbalanced Young's stress, i.e., surface tension and contact angle. Note that the range of  $\lambda$  that can be realistic-

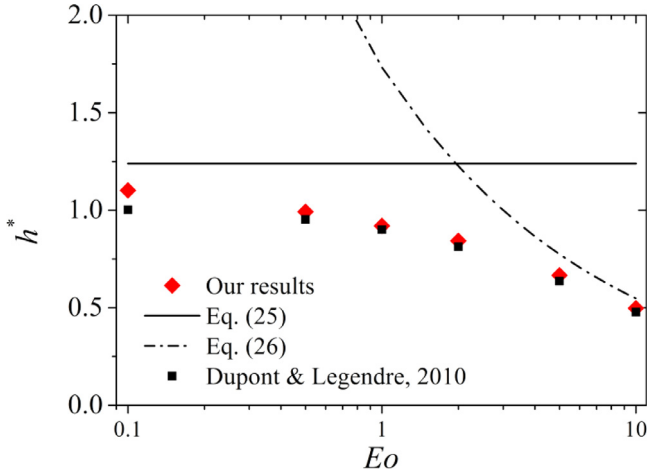


Fig. 17. Normalized height  $h^* = h_d/R$  of a droplet resting on a hydrophilic wall ( $\theta_e = 3\pi/2$ ) under the effect of gravity, where the squared points are the results from Dupont and Legendre [61].

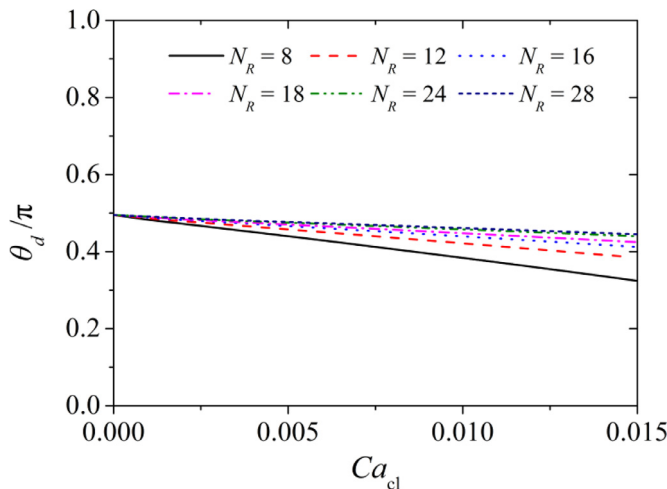


Fig. 18. Evolution of the dynamic contact angle  $\theta_d$  versus the capillary number  $Ca_{cl}$  defined by the contact line speed at  $\lambda = 0.01$ .

cally simulated is limited. Fortunately, the multi-resolution mesh method can be used to simulate the system at small  $\lambda$  [60].

Numerical tests were conducted to verify the reliability and robustness of our method. The performance of the FT method in simulating the suspended droplet with a viscoelastic interface was validated previously [29,30]. In this section, a droplet (initially with a uniform contact angle  $\theta_0$ ) adhering to a solid surface in linear shear flows is tracked, in which the effect of upper confining wall is ignored. Unless otherwise noted, all simulations were conducted at  $Re = 0.1$ ,  $Ca = 0.1$ , and  $\lambda = 0.01$ . The computational domain size  $L_x \times L_y \times L_z$  is  $12R \times 5R \times 5R$ , and the droplet is placed at the position of  $x = 4R$ .

The deformation of the droplet decreases when the Eulerian mesh is refined. As shown in Fig. 19, these numerical results are accurate with an error of less than 4.5% for the coarsest mesh compared with the result for the finest mesh (i.e.,  $N_R = 28$ ), and the error is only 0.8% for the Eulerian mesh resolution of  $N_R = 18$ . The use of various-resolution Lagrangian mesh reveals that  $N_e = 4608$  at the initial time is sufficient to track the interface. In this case, the number of contact line marker points is 96. The steady-state contact angles computed at each contact line marker are shown in Fig. 20. The steady-state contact angle at the end of the upstream contact line only increases by up to 2% as  $N_R$  varies from

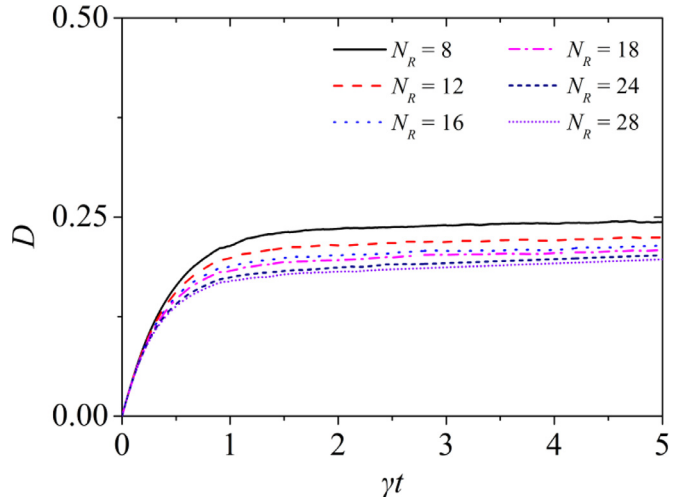


Fig. 19. Numerical performance tests by simulating deformation of a droplet with moving contact line for varying Eulerian resolution.

18 to 24. Unless otherwise stated, the obtained results in the following sections are all performed at  $N_R = 18$ .

Because of the contact lines movement has significant effect on the deformation of the droplet on a solid surface, we compared our results with two-dimensional simulation by the FT method using a classical slip model (i.e., NBC) [24], in which the static contact angle model was applied. The density ratio is  $k_\rho = 10$  and  $\lambda = 0.0125$  (the characteristic length is height of the parallel-walled channel in Ref. [24]). The capillary number  $Ca$  varies from 0 to 0.16. Fig. 21 displays the steady-state shape for a droplet moving on the solid surface. The result using the NBC have a little different with our results as the interfacial profiles indicated in Fig. 21, in which the deformation of droplet is more pronounced in the XZ plane. If the value of slip length actually employed in Zhang et al. [24] is available, our results would show better agreement. In this case, the GNBC can be comparable to other empirical correlations under certain conditions.

#### 4.5. Contact angle hysteresis

The effect of contact angle hysteresis on the droplet dynamics has received increasing attention [61–64]. In our method, this effect has been considered in the GNBC. Here, we consider a droplet resting on the solid surface with an initial contact angle  $\theta_0 = \pi/2$ . Note that the value  $Ca = 0.2$  and  $Re = 0.1$  are used in this section for  $\lambda = 0.01$ . We first consider the case of advancing contact angle  $\theta_A = \theta_0$ . As shown in Fig. 22(a), in the case of  $\theta_R = 7\pi/18$ , we clearly observe that the receding contact line immediately moves once the droplet deforms. Meanwhile, the advancing contact line immediately starts to move once the advancing contact angle exceeds the lower limit  $\theta_R$ . Then the local contact angle  $\theta_{up}$  can be finally reached a constant value. Besides, evolution of the shape shown in Fig. 23(a) also reveals that a steady-state shape can be obtained for a small hysteresis.

For the case of  $(\theta_A, \theta_R) = (\pi/3, 2\pi/3)$ , the advancing and receding contact lines are all immobile until the interface deforms to reach their corresponding limit values  $\theta_A$  and  $\theta_R$ . In addition to the capillary number  $Ca$ , the hysteresis condition also has a great effect on the shape of the droplet. The deformation of the droplet increasing with increasing the hysteresis. According to the reports by the previous literatures, there is a corresponding increase in the critical capillary number to reach the steady state at the large hysteresis [21]. The corresponding evolutions of the local Capillary number  $Ca_{cl}$  based on the velocity of the contact line reported in

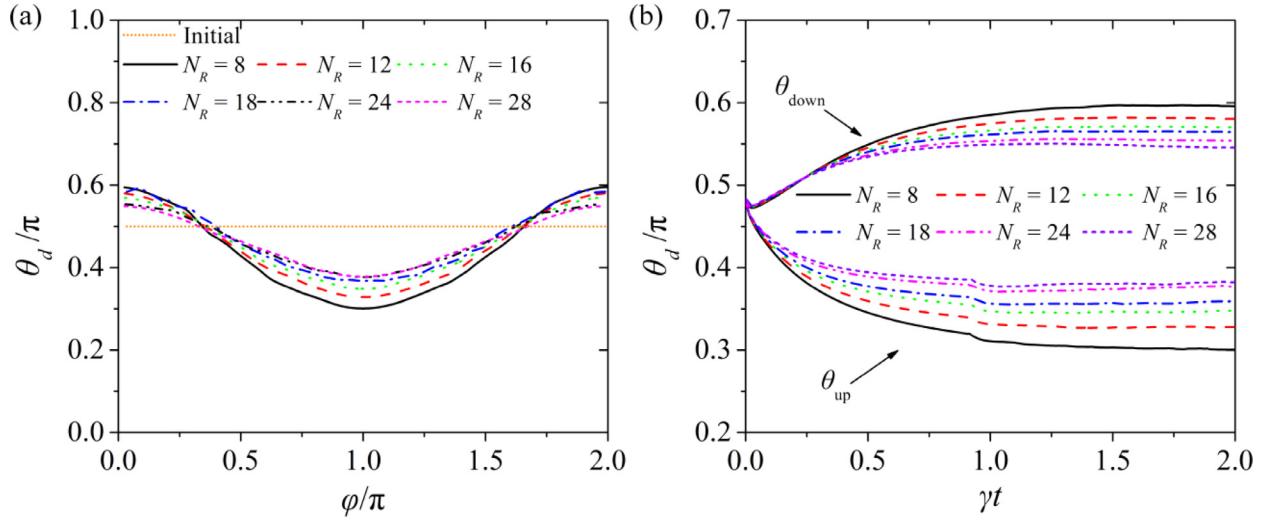


**Fig. 20.** Dynamic contact angle profiles along the contact line in the counterclockwise direction (left). Right: evolution of the contact angle at  $\varphi = \pi$  for different values of  $N_R$ . Here  $\varphi$  is the position of the discrete contact line marker point relative to the center position of the area enclosed by the contact line. Note that  $\varphi = 0$  and  $\varphi = \pi$  are the positions at the end of the downstream and upstream contact line, respectively.

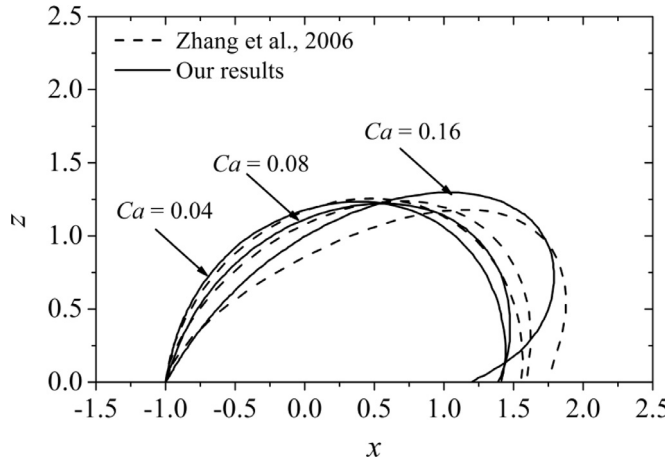


**Fig. 21.** The steady-state shapes of a droplet with  $\theta_0 = \pi/2$  in shear flow with  $Ca = 0.04, 0.08$  and  $0.16$ . Here, the GNBC is applied for the contact line when it moves on the solid surface. The short-dashed lines are droplet profiles tracked with the two-dimensional FT method, in which the NBC and a constant contact angle were applied [24].

Fig. 22 also prove that the hysteresis model used in the present method is correct. Besides, it is found the velocity difference between the advancing and receding contact lines increases with the hysteresis increasing. For a large hysteresis with  $(\theta_A, \theta_R) = (\pi/2, 15\pi/18)$ , the receding contact line even moves faster than the advancing contact line. Comprehensive consideration of its corresponding evolution of shape in Fig. 23(c), the droplet has a tendency to be detached by the surrounding fluid.

## 5. Conclusions

Although the FT method has good overall performance in determining the precise location of contact lines in three dimensions, reports of multiphase modeling with contact line dynamics using FT-type methods are relatively scarce. This is largely due to the complexity of relinking unstructured triangular mesh. This can be very important and essential in three-dimensional simulations where the fluid interface must be reconstructed. In addition, the empirical correlations from experimental results are usually interested in the macroscopic behavior of interfacial deformation near

the contact line, which cannot be associated to the interface deformation without considering the coupled effect of interfacial properties on the contact line dynamics. Numerical implementation of a complete description that accounts for the complex interfacial physics associated with the contact line remains a formidable task.

In this paper, we develop a three-dimensional FT method to simulate the motion of droplets on a solid surface. For multiphase modeling with contact line dynamics, we use the GNBC to alleviate stress singularities and completely describe the behaviors of the contact line by considering the unbalanced Young's force as a stress on the solid surface and taking CAH into account. To obtain a well-structured interface consisting of uniformly distributed triangular mesh with high quality, restructuring techniques are applied to link the Lagrangian mesh with the contact line. The error induced by restructuring is negligible based on calculations of the surface tension, contact angle and total deformation of the interface. In addition, the resulting indicator function field near the contact line is quite continuous, and its gradient can be directly used to calculate the local contact angle without further modification of the procedure. The application of GNBC to describe the dynamics of contact line can directly account for complex interfacial properties, for instance, temporal variation of the surface tension in a solution of surfactants, non-Newtonian fluid. Theoretically, the implementation of such a contact line model is relatively straightforward and extensible, especially for the 3D explicit interface tracking methods.

A number of tests were performed to validate the numerical performance. The simulation of a sessile droplet showed good agreement with the analytic solution, with errors of less than 0.4%, indicating that the surface tension calculation procedure is accurate. A numerical convergence test indicated convergence of the surface tension calculation and the contact line model. Two types of simulations associated with the contact line were performed. The first showed the deformation of a droplet adhering to a solid surface with fixed contact lines under a shear flow, and the results were in good agreement with the previous solutions for the instantaneous and steady-state cases. The second type of simulation, which was conducted for a droplet spreading under gravity and moving under a shear flow with moving contact lines, showed good agreement with other results. Overall, the developed method can be used to simulate a number of problems involving the contact line.

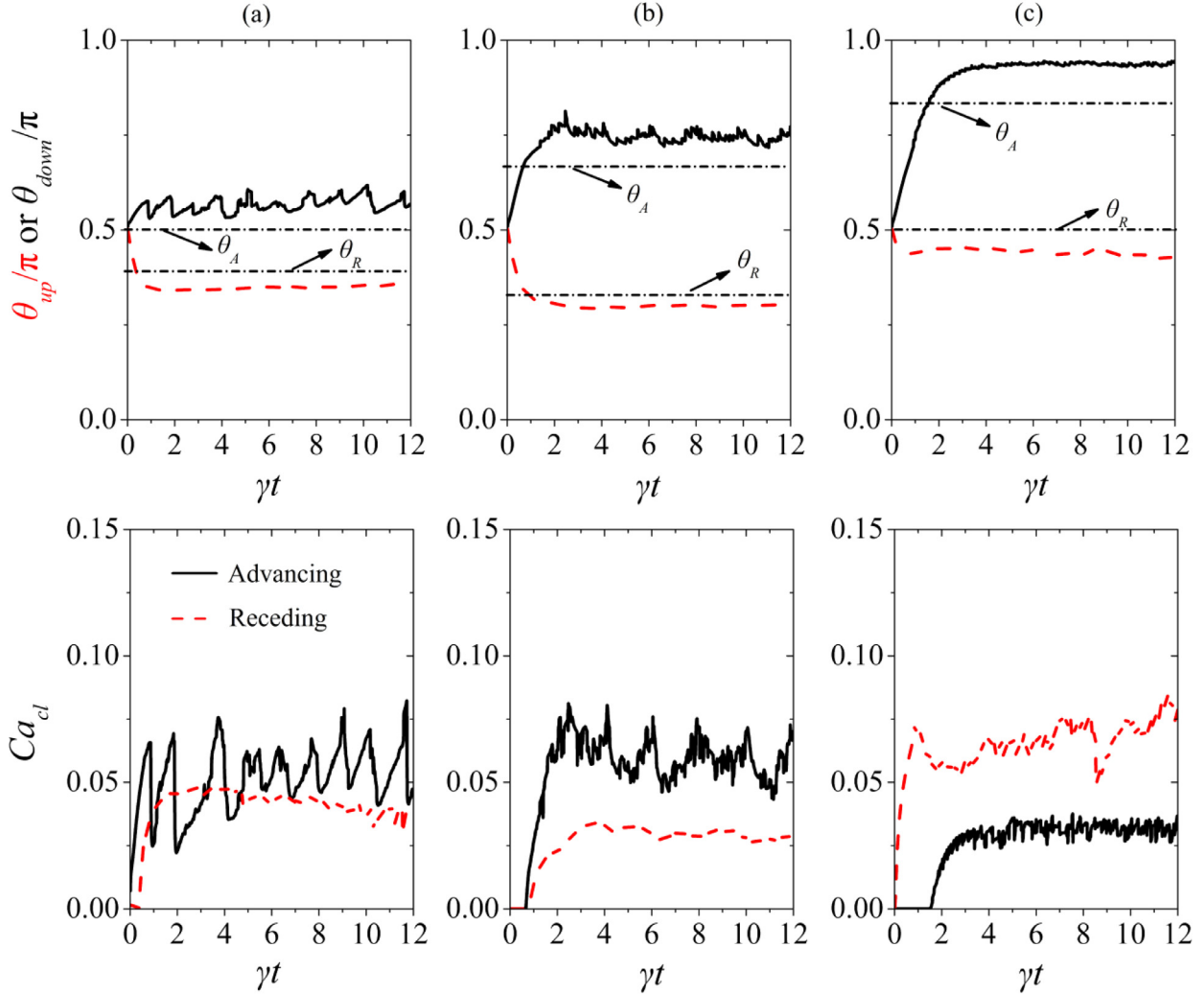


**Fig. 22.** Advancing and receding contact angles  $\theta_{up}$  (dashed lines),  $\theta_{down}$  (solid lines) and the local Capillary number  $Ca_{cl}$  based on the velocity of the contact line versus time for (a)  $(\theta_A, \theta_R) = (7\pi/18, \pi/2)$ , (b)  $(\theta_A, \theta_R) = (\pi/3, 2\pi/3)$  and (c)  $(\theta_A, \theta_R) = (\pi/2, 15\pi/18)$ .

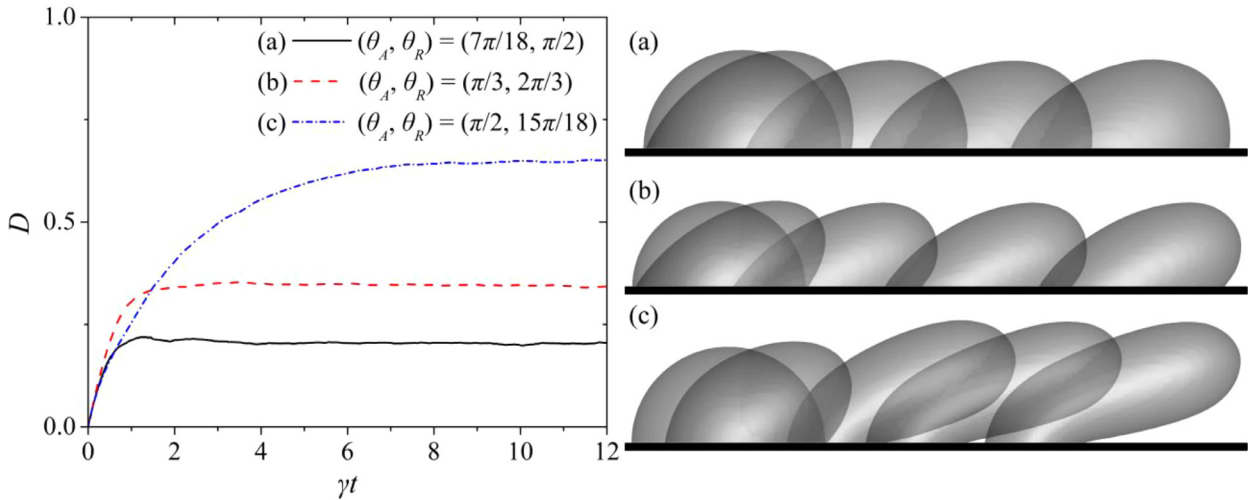


**Fig. 23.** Evolutions of the deformation parameter  $D$  of the droplet and their corresponding snapshots of shape for (a)  $(\theta_A, \theta_R) = (7\pi/18, \pi/2)$ , (b)  $(\theta_A, \theta_R) = (\pi/3, 2\pi/3)$  and (c)  $(\theta_A, \theta_R) = (\pi/2, 15\pi/18)$ .

## Acknowledgment

Bofeng Bai acknowledges financial support from the Ministry of Science and Technology (2017YFE0100600) and the National Science Fund for Distinguished Young Scholars of China (51425603). Oleg A. Kabov and Elizaveta Ya. Gatapova acknowledge financial support from the Ministry of Education and Science of the Russian Federation (RFMEFI61317X0067).

## References

- [1] Bonn D, Eggers J, Indekeu J, Meunier J, Rolley E. Wetting and spreading. *Rev Mod Phys* 2009;81:739–805.
- [2] Sui Y, Ding H, Spelt PDM. Numerical simulations of flows with moving contact lines. *Annu Rev Fluid Mech* 2014;46:97–119.
- [3] Snoeijer JH, Andreotti B. Moving contact lines: scales, regimes, and dynamical transitions. *Annu Rev Fluid Mech* 2013;45:269–292.
- [4] Wörner M. Numerical modeling of multiphase flows in microfluidics and micro process engineering: a review of methods and applications. *Microfluid Nanofluid* 2012;12:841–886.
- [5] Dussan VEB. On the dynamics of liquid spreading on solid surfaces. *J Fluid Mech* 1989;209:191–226.
- [6] Kistler SF. In: Berger JC, editor. *Hydrodynamics of wetting*. New York: Marcel Dekker; 1993. p. 311–429. Wettability.
- [7] Jiang T, Soogun O, Slattery J. Correlation for dynamic contact angle. *J Colloid Interface Sci* 1979;69:74–77.
- [8] Qian T, Wang X-P, Sheng P. Generalized Navier boundary condition for the moving contact line. *Commun Math Sci* 2003;1:333–341.
- [9] Kralchevsky PA, Danov KD, Kolev VL, Gurkov TD, Temelska MI, Brenn G. Detachment of oil drops from solid surfaces in surfactant solutions: molecular mechanisms at a moving contact line. *Ind Eng Chem Res* 2005;44:1309–1321.
- [10] Ren W. Contact line dynamics on heterogeneous surfaces. *Phys Fluids* 2011;23:072103.
- [11] Ajayev VS, Gatapova EY, Kabov OA. Stability and break-up of thin liquid films on patterned and structured surfaces. *Adv Colloid Interface Sci* 2016;228:92–104.
- [12] Ramos S, Charlaix E, Benyagoub A, Toulemonde M. Wetting on nanorough surfaces. *Phys Rev E* 2003;67:031604.
- [13] Ajayev VS, Gatapova EY, Kabov OA. Application of Floquet theory to the stability of liquid films on structured surfaces. *Phys Fluids* 2013;25:122102.
- [14] Kabova YO, Alexeev A, Gambaryan-Roisman T, Stephan P, Marangoni-induced deformation and rupture of a liquid film on a heated microstructured wall. *Phys Fluids* 2006;18:012104.
- [15] Petrov JG, Ralston J, Schneemilch M, Hayes RA. Dynamics of partial wetting and dewetting in well-defined systems. *J Phys Chem B* 2003;107:1634–1645.
- [16] Afkhami S, Zaleski S, Bussmann M. A mesh-dependent model for applying dynamic contact angles to VOF simulations. *J Comput Phys* 2009;228:5370–5389.
- [17] Sikalo S, Wilhelm HD, Roisman IV, Jakirlić S, Tropea C. Dynamic contact angle of spreading droplets: experiments and simulations. *Phys Fluids* 2005;17:062103.
- [18] Spelt PDM. A level-set approach for simulations of flows with multiple moving contact lines with hysteresis. *J Comput Phys* 2005;207:389–404.
- [19] Deganello D, Croft TN, Williams AJ, Lubansky AS, Gethin DT, Claypole TC. Numerical simulation of dynamic contact angle using a force based formulation. *J Non-Newton Fluid* 2011;166:900–907.
- [20] Ding H, Gilani MNH, Spelt PDM. Sliding, pinch-off and detachment of a droplet on a wall in shear flow. *J Fluid Mech* 2010;644:217–244.
- [21] Ding H, Spelt PD. Onset of motion of a three-dimensional droplet on a wall in shear flow at moderate Reynolds numbers. *J Fluid Mech* 2008;599:341–362.
- [22] Yue P, Zhou C, Feng JJ. Sharp-interface limit of the Cahn–Hilliard model for moving contact lines. *J Fluid Mech* 2010;645:279–294.
- [23] Li Z, Lai M, He G, Zhao H. An augmented method for free boundary problems with moving contact lines. *Comput Fluids* 2010;39:1033–1040.
- [24] Zhang J, Miksis M, Bankoff S. Nonlinear dynamics of a two-dimensional viscous drop under shear flow. *Phys Fluids* 2006;18:072106.
- [25] Manservisi S, Scardovelli R. A variational approach to the contact angle dynamics of spreading droplets. *Comput Fluids* 2009;38:406–424.
- [26] Muradoglu M, Tasoglu S. A front-tracking method for computational modeling of impact and spreading of viscous droplets on solid walls. *Comput Fluids* 2010;39:615–625.
- [27] Huang H, Liang D, Wetton B. Computation of a moving drop/bubble on a solid surface using a front-tracking method. *Commun Math Sci* 2004;2:535–552.
- [28] Yamamoto Y, Ito T, Wakimoto T, Katoh K. Numerical simulations of spontaneous capillary rises with very low capillary numbers using a front-tracking method combined with generalized Navier boundary condition. *Int J Multiph Flow* 2013;51:22–32.
- [29] Luo ZY, Bai BF. Dynamics of nonspherical compound capsules in simple shear flow. *Phys Fluids* 2016;28:101901.
- [30] Luo ZY, He L, Bai BF. Deformation of spherical compound capsules in simple shear flow. *J Fluid Mech* 2015;775:77–104.
- [31] Bai BF, Luo ZY, Wang SQ, He L, Lu TJ, Xu F. Inertia effect on deformation of viscoelastic capsules in microscale flows. *Microfluid Nanofluid* 2012;14:817–829.
- [32] Qian T, Wang X, Sheng P. Molecular scale contact line hydrodynamics of immiscible flows. *Phys Rev E* 2003;68:016306.
- [33] Peskin CS. The immersed boundary method. *Acta Numer* 2003;11:479–517.
- [34] Huh C, Mason SG. The steady movement of a liquid meniscus in a capillary tube. *J Fluid Mech* 1977;81:401–419.
- [35] Ni M-J, Komori S, Morley N. Projection methods for the calculation of incompressible unsteady flows. *Numer Heat Trans B-Fund* 2003;44:533–551.
- [36] Trottenberg U, Oosterlee C, Schüller A. *Multigrid*. London: Academic Press; 2001.
- [37] Li Y, Yun A, Lee D, Shin J, Jeong D, Kim J. Three-dimensional volume-conserving immersed boundary model for two-phase fluid flows. *Comput Method Appl M* 2013;257:36–46.
- [38] Esmaeeli A, Tryggvason G. Direct numerical simulations of bubbly flows. Part 1. Low Reynolds number arrays. *J Fluid Mech* 1998;377:313–345.
- [39] Tryggvason G, Bunner B, Esmaeeli A, Juric D, Al-Rawahi N, Tauber W, et al. A front-tracking method for the computations of multiphase flow. *J Comput Phys* 2001;169:708–759.
- [40] Unverdi SO, Tryggvason G. A front-tracking method for viscous, incompressible, multi-fluid flows. *J Comput Phys* 1992;100:25–37.
- [41] Thompson PA, Brinckerhoff W, Robbins MO. Microscopic studies of static and dynamic contact angles. *J Adhes Sci Technol* 1993;7:535–554.
- [42] Cox RG. The dynamics of the spreading of liquids on a solid surface. Part 1. Viscous flow. *J Fluid Mech* 1986;168:169–194.
- [43] Cox RG. The dynamics of the spreading of liquids on a solid surface. Part 2. Surfactants. *J Fluid Mech* 1986;168:195–220.
- [44] Yamamoto Y, Higashida S, Tanaka H, Wakimoto T, Ito T, Katoh K. Numerical analysis of contact line dynamics passing over a single wettable defect on a wall. *Phys Fluids* 2016;28:082109.
- [45] Hancock MJ, Sekeroglu K, Demirel MC. Bioinspired directional surfaces for adhesion, wetting, and transport. *Adv Funct Mater* 2012;22:2223–34.
- [46] Pitt WG. Fabrication of a continuous wettability gradient by radio frequency plasma discharge. *J Colloid Interf Sci* 1989;133:223–7.
- [47] Kavousanakis ME, Colosqui CE, Papathanasiou AG. Engineering the geometry of stripe-patterned surfaces toward efficient wettability switching. *Colloids Surf A* 2013;436:309–317.
- [48] Bliznyuk O, Jansen HP, Kooij ES, Zandvliet HJW, Poelsema B. Smart design of stripe-patterned gradient surfaces to control droplet motion. *Langmuir* 2011;27:11238–45.
- [49] Yue W, Guo Q, Zhang J, Wang G. 3D triangular mesh optimization in geometry processing for CAD. In: *Proceedings of the 2007 ACM symposium on solid and physical modeling*. ACM; 2007. p. 23–33.
- [50] Mari JF, Saito JH, Poli G, Zorzan MR, Levada AL. Improving the neural meshes algorithm for 3D surface reconstruction with edge swap operations. In: *Proceedings of the 2008 ACM symposium on applied computing*. ACM; 2008. p. 1236–40.
- [51] Yu Z, Holst MJ, Mccammon JA. High-fidelity geometric modeling for biomedical applications. *Finite Elem Anal Des* 2008;44:715–723.
- [52] Page DL, Sun Y, Koschan A, Paik J, Abidi MA. Normal vector voting: crease detection and curvature estimation on large, noisy meshes. *Graph Models* 2002;64:199–229.
- [53] Gao Z, Yu Z, Holst M. Feature-preserving surface mesh smoothing via suboptimal Delaunay triangulation. *Graph Models* 2013;75:23–38.
- [54] Khennar M. Computation of the material indicator function near the contact line (in Tryggvason's method). *J Comput Phys* 2004;200:1–7.
- [55] Brackbill J, Kothe DB, Zemach C. A continuum method for modeling surface tension. *J Comput Phys* 1992;100:335–354.
- [56] Sugiyama K, Sbragaglia M. Linear shear flow past a hemispherical droplet adhering to a solid surface. *J Eng Math* 2007;62:35–50.
- [57] Li X, Pozrikidis C. Shear flow over a liquid drop adhering to a solid surface. *J Fluid Mech* 1996;307:167–190.
- [58] Dimitrakopoulos P. Deformation of a droplet adhering to a solid surface in shear flow: onset of interfacial sliding. *J Fluid Mech* 2007;580:451–466.
- [59] Ehrhard P, Davis SH. Non-isothermal spreading of liquid drops on horizontal plates. *J Fluid Mech* 1991;229:365–88.
- [60] Pivello MR, Villar MM, Serfaty R, Roma AM, Silveira-Neto A. A fully adaptive front tracking method for the simulation of two phase flows. *Int J Multiph Flow* 2014;58:72–82.
- [61] Dupont JB, Legendre D. Numerical simulation of static and sliding drop with contact angle hysteresis. *J Comput Phys* 2010;229:2453–78.
- [62] Park JK, Kang KH. Numerical analysis of moving contact line with contact angle hysteresis using feedback deceleration technique. *Phys Fluids* 2012;24:042105.
- [63] Fang C, Hidrovo C, Wang F, Eaton J, Goodson K. 3-D numerical simulation of contact angle hysteresis for microscale two phase flow. *Int J Multiph Flow* 2008;34:690–705.
- [64] Eral HB, Oh JM. Contact angle hysteresis: a review of fundamentals and applications. *Colloid Polym Sci* 2012;291:247–60.